

This work was written as part of one of the author's official duties as an Employee of the United States Government and is therefore a work of the United States Government. In accordance with 17 U.S.C. 105, no copyright protection is available for such works under U.S. Law.

Public Domain Mark 1.0

<https://creativecommons.org/publicdomain/mark/1.0/>

Access to this work was provided by the University of Maryland, Baltimore County (UMBC) ScholarWorks@UMBC digital repository on the Maryland Shared Open Access (MD-SOAR) platform.

**Please provide feedback**

Please support the ScholarWorks@UMBC repository by emailing [scholarworks-group@umbc.edu](mailto:scholarworks-group@umbc.edu) and telling us what having access to this work means to you and why it's important to you. Thank you.

## The Rapid Intensification of Hurricane Karl (2010): New Remote Sensing Observations of Convective Bursts from the Global Hawk Platform

STEPHEN R. GUIMOND

*Earth System Science Interdisciplinary Center, University of Maryland, College Park, College Park, and NASA  
Goddard Space Flight Center, Greenbelt, Maryland*

GERALD M. HEYMSFIELD

*NASA Goddard Space Flight Center, Greenbelt, Maryland*

PAUL D. REASOR

*NOAA/Atlantic Oceanographic and Meteorological Laboratory/Hurricane Research Division, Miami, Florida*

ANTHONY C. DIDLAKE JR.

*NASA Goddard Space Flight Center, Greenbelt, Maryland, and Oak Ridge Associated Universities, Oak Ridge, Tennessee*

(Manuscript received 14 January 2016, in final form 22 June 2016)

### ABSTRACT

The evolution of rapidly intensifying Hurricane Karl (2010) is examined from a suite of remote sensing observations during the NASA Genesis and Rapid Intensification Processes (GRIP) field experiment. The novelties of this study are in the analysis of data from the airborne Doppler radar High-Altitude Imaging Wind and Rain Airborne Profiler (HIWRAP) and the new Global Hawk airborne platform that allows long endurance sampling of hurricanes. Supporting data from the High-Altitude Monolithic Microwave Integrated Circuit (MMIC) Sounding Radiometer (HAMSR) microwave sounder coincident with HIWRAP and coordinated flights with the NOAA WP-3D aircraft help to provide a comprehensive understanding of the storm. The focus of the analysis is on documenting and understanding the structure, evolution, and role of small-scale deep convective forcing in the storm intensification process. Deep convective bursts are sporadically initiated in the downshear quadrants of the storm and rotate into the upshear quadrants for a period of  $\sim 12$  h during the rapid intensification. The aircraft data analysis indicates that the bursts are being formed and maintained through a combination of two main processes: 1) convergence generated from counterrotating mesovortex circulations and the larger vortex-scale flow and 2) the turbulent (scales of  $\sim 25$  km) transport of anomalously warm, buoyant air from the eye to the eyewall at low levels. The turbulent mixing across the eyewall interface and forced convective descent adjacent to the bursts assists in carving out the eye of Karl, which leads to an asymmetric enhancement of the warm core. The mesovortices play a key role in the evolution of the features described above. The Global Hawk aircraft allowed an examination of the vortex response and axisymmetrization period in addition to the burst pulsing phase. A pronounced axisymmetric development of the vortex is observed following the pulsing phase that includes a sloped eyewall structure and formation of a clear, wide eye.

### 1. Introduction

The intensification of tropical cyclones (TCs) is a complex process that is governed by nonlinear coupling of physics across a vast array of space and time scales.

On the slow/large scales, a sufficiently warm ocean and low vertical wind shear have been identified as providing favorable environmental conditions for the intensification of TCs (e.g., [Kaplan and DeMaria 2003](#)). On the fast/small scales, a large body of evidence has shown that deep, rotating, convective towers are responsible for the intensification, including rapid intensification (RI), of TCs ([Steranka et al. 1986](#); [Simpson et al. 1998](#); [Heymsfield et al. 2001](#); [Kelley et al.](#)

---

*Corresponding author address:* Stephen R. Guimond, NASA Goddard Space Flight Center, Code 612, Greenbelt, MD 20771.  
E-mail: [stephen.guimond@nasa.gov](mailto:stephen.guimond@nasa.gov)

2004; Montgomery et al. 2006; Braun et al. 2006; Reasor et al. 2009; Guimond et al. 2010; Molinari and Vollaro 2010; Rogers et al. 2015). However, recent studies by Jiang (2012) and Tao and Jiang (2015), using statistics from a large satellite database, have stated that shallow and moderate precipitation is more important for the RI process than deep convective precipitation. Uncertainty remains in these satellite-based studies as a result of the inherently coarse temporal (and spatial) resolution for analyzing the cloud/precipitation life cycle as well as the definition of RI relative to other studies.

It is the fast/small scales that are the most challenging for the observation, numerical modeling, and understanding of TCs. Deep convective towers in TCs have lifetimes of an hour or less with horizontal scales of  $\sim 10$  km (Montgomery et al. 2006; Houze et al. 2009; Guimond et al. 2010), making it difficult to observe their kinematic properties, especially from conventional aircraft, which can only sample storms for short periods of time ( $\sim 5$  h). The turbulent, highly nonlinear character of deep convective towers and their interaction with the TC vortex are major challenges for numerical models and our physical understanding because those scales not explicitly resolved must be parameterized, which are not always adequate (e.g., Persing et al. 2013) and there can be considerable sensitivity to the algorithms used to solve the fluid-flow equations (e.g., Guimond et al. 2016, manuscript submitted to *J. Atmos. Sci.*).

The dynamics responsible for the rapid intensification of TCs from localized, deep convection project onto two classes of modes relative to the storm center: axisymmetric and asymmetric. In the axisymmetric framework, the projection of localized heat forcing onto the azimuthal mean results in rings of heating typically maximized inside the radius of maximum winds for intensifying storms. Rogers et al. (2013) analyzed a large set of airborne Doppler radar composites of intensifying and steady-state TCs and discovered that a key characteristic of intensifying TCs is the location of deep convective towers inside the radius of maximum winds (RMW). Earlier studies by Schubert and Hack (1982), Nolan et al. (2007), and Vigh and Schubert (2009) have elucidated the dynamics of intensifying hurricane vortices, finding that convective heating placed inside the RMW enables more efficient conversion of potential to kinetic energy owing to the increased inertial stability of the vortex.

The heating rings drive an axisymmetric secondary circulation with radial inflow at low levels, updrafts through the core of the heating, and radial outflow aloft. In the azimuthal mean, the vortex intensifies through the radial convergence of absolute angular momentum,

which is materially conserved above the boundary layer. This framework has been understood for many years (e.g., Shapiro and Willoughby 1982). Other axisymmetric theories for TC intensification have been presented such as the work of Emanuel (1986) and Rotunno and Emanuel (1987), which focus on the cycling of energy extracted through the thermodynamic disequilibrium at the air–ocean interface.

In the asymmetric framework, the heating and vorticity asymmetries generated from localized convective forcing interact with the mean flow through eddy heat and momentum fluxes, which can lead to intensification of the vortex for upgradient transport (Montgomery and Kallenbach 1997). This process is generally called “axisymmetrization” and has been shown to occur in observational (e.g., Reasor et al. 2000, 2009) and modeling (e.g., Montgomery et al. 2006; Persing et al. 2013) studies. In nature, the axisymmetric and asymmetric modes are coupled to one another with axisymmetric processes often playing the largest role (e.g., Nolan and Grasso 2003), but with asymmetric dynamics contributing a significant, nonnegligible component of the overall system intensification (e.g., Montgomery et al. 2006; Persing et al. 2013; Guimond et al. 2016, manuscript submitted to *J. Atmos. Sci.*).

In addition to these effects, deep convective towers have also been observed to initiate localized interaction between the eye and eyewall. For example, the studies of Heymsfield et al. (2001) and Guimond et al. (2010), which analyzed very-high-resolution airborne radar data (along-track sampling of 100 m), showed that deep convective towers intensified the warm core through compensating subsidence around strong updrafts and its turbulent transport toward the eye. This intense, localized transport of air from the eyewall to the eye has important implications for storm intensification through the attendant inward flux of angular momentum. Finally, Wang and Wang (2014) simulated the intensification of Typhoon Megi (2010) and found that convective bursts in the eyewall helped to intensify the TC warm core at upper levels by detraining high potential temperature air from the stratosphere.

The purpose of this paper is to analyze the RI of Hurricane Karl (2010), which coincided with a convective burst episode, from a suite of remote sensing observations to understand more details of the dynamics occurring on the fast/small scales. The novelties of this study are in the use of a new airborne radar and a new airborne platform for hurricane research that allows long endurance (up to 24 h) sampling. Details of these new technologies will be discussed in the next section.

## 2. Data and processing

### a. HIWRAP

The High-Altitude Imaging Wind and Rain Airborne Profiler (HIWRAP) is an airborne Doppler radar that was developed at the NASA Goddard Space Flight Center (GSFC) with the goal of studying hurricanes and other precipitating systems. One of the unique features of HIWRAP is its ability to fly on NASA's Global Hawk (GH) unmanned aircraft, which operates at  $\sim 18$ – $19$ -km (60–62 kft) altitude and can remain airborne for  $\sim 24$  h. The long endurance of the GH is a significant capability for hurricane research. Hurricanes form over remote regions of the ocean with important physical processes occurring on fast time scales that can be easily missed by conventional aircraft that can only remain airborne for  $\sim 6$  h. Satellite measurements can reach these remote areas, but the observational capabilities, including spatial/temporal sampling, is less than optimal.

HIWRAP is a dual-frequency (Ku and Ka band), single-polarized (vertical for inner beam, horizontal for outer beam), downward-pointing and conically scanning (16 rpm) Doppler radar with two beams ( $\sim 30^\circ$  and  $40^\circ$  tilt angles) and 150-m-range resolution. The GH aircraft has an airspeed of  $\sim 160 \text{ m s}^{-1}$ , which yields  $\sim 600$ -m along-track sampling for HIWRAP. More details on HIWRAP can be found in [Li et al. \(2016\)](#).

The NASA Genesis and Rapid Intensification Processes (GRIP) experiment in 2010 was the first time HIWRAP collected significant data and some issues with the data quality (e.g., excessive noise at Ku band due to a variety of issues including pulse processing) were found. To address these issues, we have done two things: 1) pulse pair estimates at Ku band were reprocessed with 128 pulses averaged (azimuthal resolution of  $\sim 2.8^\circ$ ), which improves the signal-to-noise ratio (SNR) over the original averaging interval of 64 pulses, and 2) Ku-band wind retrievals below the noise saturation level (determined using a power threshold, which translates to  $\sim 25$  dBZ at 3-km height) were replaced with the corresponding Ka-band wind retrievals, which provide a higher SNR and, thus, lower uncertainty in the Doppler velocities in these regions. In the flights over Karl presented in this work, only the inner ( $30^\circ$ ) beam was functional, which provides a swath width at the surface of  $\sim 20$ – $22$  km.

Retrievals of the three-dimensional wind vector over the entire radar-sampling volume are performed with the three-dimensional variational data assimilation (3DVAR) algorithm described in [Guimond et al. \(2014\)](#). The 3DVAR method combines an observational error term as well as constraints that include the anelastic mass continuity equation, a Laplacian filter, and the

impermeability condition at the surface. No background field is included in the algorithm because a quality wind field can be obtained using the observations and dynamic constraints alone. A coefficient of  $2\Delta x^2$  was used for the mass continuity constraint and  $0.5\Delta x^4$  was used for the filtering constraint with  $\Delta x$  representing the horizontal grid spacing. These values were chosen based on wind vector solution sensitivity tests that provided reasonable accuracy and damping characteristics. The retrievals are performed on a storm-following grid with a horizontal grid spacing of 1 km and vertical spacing of 1 km. Retrievals with vertical spacing of  $\sim 150$  m are possible, but 1-km spacing was deemed sufficient for the present study. The first level of useful data is  $\sim 1$ -km height for the inner beam. Below this height, antenna side lobes interacting with the surface obscure the precipitation signal. NOAA's Hurricane Research Division (HRD), using the [Willoughby and Chelmow \(1982\)](#) method, provided storm center estimates. The mean storm motion vector averaged over the aircraft-sampling period was removed from the HIWRAP-derived horizontal winds.

[Guimond et al. \(2014\)](#) showed that simulated and in situ errors for the horizontal wind components were  $\sim 2.0 \text{ m s}^{-1}$  or  $\sim 7\%$  of the hurricane wind speed. The errors in the vertical velocity were strongly dependent on the across-track location of the measurements with comparisons to in situ data revealing errors of  $\sim 2.0 \text{ m s}^{-1}$  at nadir. Simulated off-nadir vertical velocity estimates were still quite accurate within  $\pm 5$  km from nadir ([Guimond et al. 2014](#)). The in situ errors noted above used data from the Imaging Wind and Rain Airborne Profiler (IWRAP) flying on the NOAA WP-3D aircraft, which has a similar scanning geometry to HIWRAP. The [appendix](#) presents comparisons of in situ data to HIWRAP retrievals, which reveal that for wind speeds  $> 10 \text{ m s}^{-1}$  the mean error in the computed wind speed and direction is  $\sim 1$ – $4 \text{ m s}^{-1}$  and  $\sim 10^\circ$ – $20^\circ$ , respectively.

### b. NOAA WP-3D radars

The NOAA WP-3D tail (TA) radar is an X-band airborne Doppler radar that scans in a cone  $20^\circ$  fore and aft of the plane perpendicular to the aircraft with a scan rate of 10 rpm and along-track sampling of fore/aft sweeps of  $\sim 1.6$  km ([Gamache et al. 1995](#)). Retrievals of the three-dimensional wind vector are performed using the variational methodology outlined in [Gamache \(1997\)](#) and [Reasor et al. \(2009\)](#) at a grid spacing of 2 km in the horizontal and 0.5 km in the vertical. Quality control procedures on the raw observations of reflectivity and radial velocity can be found in [Gamache \(2005\)](#). The mean storm motion vector averaged over

the aircraft-sampling period was removed from the TA-derived horizontal winds.

The NOAA WP-3D aircraft also carries a C-band lower fuselage (LF) radar that provides a scan of radar reflectivity every 30 s at approximately the flight-level height. These data are useful for identifying and tracking vortex- and convective-scale features of TCs close to the aircraft. The large vertical beamwidth of  $4.1^\circ$  can cause smearing of features and inadequate beam filling for ranges greater than  $\sim 60$  km (Marks 1985). Analysis of the LF data is confined to ranges less than 50 km to avoid these problems.

### c. HAMSAR

The High-Altitude Monolithic Microwave Integrated Circuit (MMIC) Sounding Radiometer (HAMSAR) is a passive microwave sounder measuring upwelling radiation from the atmosphere at frequencies sensitive to temperature ( $\sim 50$  and  $\sim 118$  GHz) and water vapor ( $\sim 183$  GHz). The intensity of convective clouds can also be estimated in regions where upwelling radiation is scattered out of the beam by ice particles, which results in anomalously low brightness temperatures (Tbs) at the instrument receiver. The HAMSAR instrument scans  $\pm 60^\circ$  across track providing a swath width of  $\sim 65$  km from the height of the GH aircraft. However, we remove data greater than  $\pm 45^\circ$  because larger errors are found beyond this range (Brown et al. 2011). The HAMSAR Tbs exhibit across-track dependence, which is due to the viewing geometry of the instrument. As the radiometer scans away from nadir, the optical pathlength becomes larger, which pushes the weighting function peak higher in altitude, inducing a cooling effect. Goldberg et al. (2001) analyzed satellite radiometer data to show that this limb effect is relatively small within the inner portion of the swath. The analysis of HAMSAR data in this paper focuses on the inner portion of the swath to avoid larger errors associated with the limb effect.

The footprint of HAMSAR at nadir from the GH altitude is  $\sim 2$  km with an increase in size as the instrument scans off nadir. The along-track sampling of HAMSAR measurements is  $\sim 250$  m. In this study, the HAMSAR Tbs are mapped to a grid with 1-km spacing to match the HIWRAP wind retrievals. The vertical resolution of the HAMSAR data is dictated by each channel's weighting function, which amounts to  $\sim 2$ – $3$ -km intervals in height. More detailed information on HAMSAR can be found in Brown et al. (2011).

## 3. Overview of Hurricane Karl

During the summer of 2010, NASA conducted the GRIP field experiment in the Atlantic Ocean basin to

study the physical processes controlling hurricane formation and intensity change. A total of three NASA aircraft were deployed during GRIP with instruments on board to measure properties of the hurricane environment and inner-core region. In this study, we focus on the inner-core aircraft (GH) and instruments (HIWRAP and HAMSAR) described in the previous section. Further information about GRIP can be found in Braun et al. (2013).

Hurricane Karl began from a combination of a tropical wave moving off the African coast and an elongated trough of low pressure situated over the southwestern North Atlantic Ocean. Figure 1 shows the best track of Karl and intensity classifications starting at 0000 UTC 14 September. Over several days' time, deep convection located near the wave axis became more organized and by 1200 UTC 14 September a tropical depression formed in the northwestern Caribbean Sea (Stewart 2011). Not long after, Karl intensified to a tropical storm and made landfall on 15 September on the Yucatan Peninsula with surface winds of  $\sim 27 \text{ m s}^{-1}$ . Karl weakened while crossing land but was able to maintain tropical storm classification ( $\sim 20 \text{ m s}^{-1}$  surface winds) with a well-organized circulation.

After emerging into the Bay of Campeche, Karl rapidly intensified from a  $\sim 20 \text{ m s}^{-1}$  tropical storm at 0600 UTC 16 September to a  $\sim 57 \text{ m s}^{-1}$  hurricane at 1200 UTC 17 September (Fig. 1). This equates to a  $\sim 37 \text{ m s}^{-1}$  increase in surface winds in a 30-h period, which is more than double the typical RI rate of  $\sim 15 \text{ m s}^{-1}$  in 24 h (Stewart 2011). Our focus in this study is the inner-core structure and dynamics during this RI episode that was sampled by the GH aircraft between  $\sim 1900$  UTC 16 September and  $\sim 0800$  UTC 17 September (see Fig. 1).

From an environmental perspective, Karl was primed for RI with high sea surface temperatures of  $\sim 30^\circ\text{C}$  in the Bay of Campeche, relatively low vertical wind shear of  $\sim 5 \text{ m s}^{-1}$  with the vector pointing mostly toward the southwest over the RI interval, and moist midlevel air. The large-scale vertical wind shear impacting the storm was determined from CIMSS satellite analyses and verified using NCEP–NCAR reanalyses.

## 4. Convective burst remote sensing observations

### a. Satellite evolution

Animations of GOES IR satellite data indicate that localized convective bursts in Karl were actively pulsing for a  $\sim 12$ -h period between 1200 UTC 16 September and 0000 UTC 17 September. After this time period, the



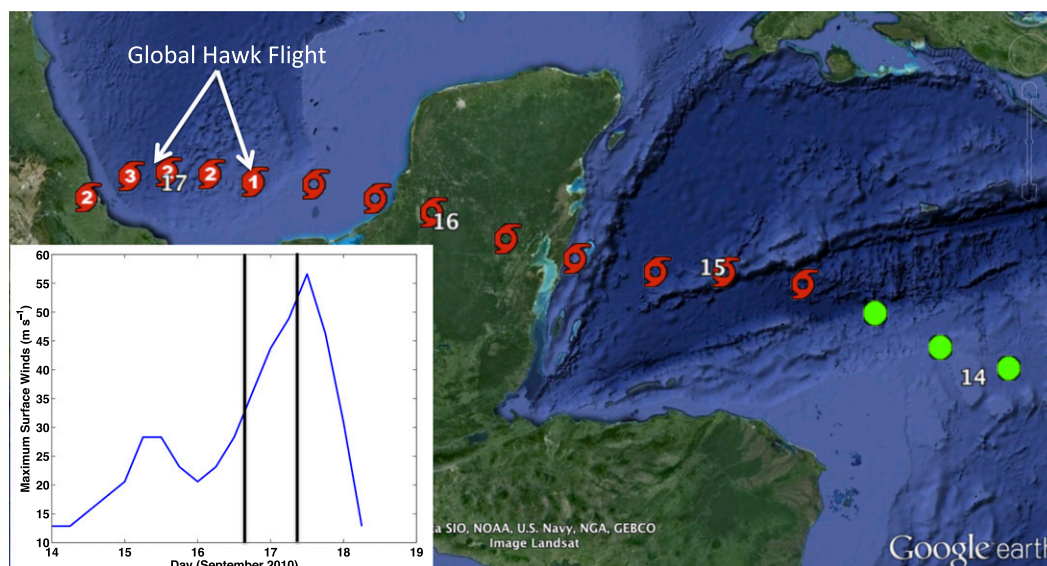


FIG. 1. Best track of Hurricane Karl (2010) starting at 0000 UTC 14 Sep with intensity classifications marked every 6 h. The days in September at 0000 UTC are also shown. The green circles denote tropical depression status, open hurricane symbols are tropical storm, and closed hurricane symbols are hurricane status with the category listed in the center. The inset shows the time series of maximum surface wind speed ( $\text{m s}^{-1}$ ) with the Global Hawk flight enclosed by the black lines.

convective forcing is less frequent and a more axisymmetric presentation of the cloud field emerges.

Figure 2 shows a sequence of GOES IR images of Karl spanning the period of GH observations during the storm's RI. The GOES IR data have a resolution of  $\sim 4$  km. At 1845 UTC 16 September (Fig. 2a), a region of asymmetric cold cloud tops ( $\sim -80^{\circ}\text{C}$ ) associated with a pulsing convective burst is located in the downshear to downshear-left portions of the storm. No apparent eye is visible at this time owing to the presence of clouds. At 2215 UTC (Fig. 2b), the convective burst episode is still evident in the IR imagery with deep convection located in the downshear-left sector of the storm and the appearance of a cloud-filled eye. A few hours later at 0140 UTC 17 September (Fig. 2c), the cold cloud-top region has wrapped around to the upshear quadrants of the storm. A clearer depiction of an eye is present at this time although it is still not cloud free. Toward the end of the aircraft observation period at 0501 UTC (Fig. 2d), the cold cloud tops have diminished and spread around the storm in a more axisymmetric pattern along with the development of a large, clear eye. Karl is nearing landfall at this point, but the core region of the storm sampled by the GH (Fig. 2d) is still well offshore (see Fig. 1).

The satellite presentation of Karl's RI with localized convective bursts pulsing in the downshear quadrants of the storm, their rotation and dissipation into the upshear quadrants, and development of an axisymmetric cloud

structure with a clear eye at late times is common (e.g., Reasor et al. 2009; Guimond et al. 2010; Stevenson et al. 2014). In addition, the presence of lightning associated with convective bursts has become more commonly recognized. Reinhart et al. (2014) analyzed satellite data and several GRIP datasets and found that some of the more intense convective burst activity in Karl produced significant lightning.

#### b. Radar time-averaged structure

The spatial and temporal evolution of convective bursts is very turbulent in nature and requires high-resolution aircraft measurements to accurately describe their structure. A time-averaged view of the storm from HIWRAP and TA radar measurements is first presented and then individual overpasses are analyzed from several data sources to highlight the detailed structure of convective bursts during the pulsing phase. Finally, we briefly show the structure of the vortex during the axisymmetric response phase.

Figure 3a shows HIWRAP Ku-band reflectivity overlaid with horizontal wind vectors at 2-km height on a storm-relative grid averaged over the entire GH sampling interval (from  $\sim 1900$  UTC 16 September to 0800 UTC 17 September). A broad cyclonic circulation is evident with a reflectivity-filled eye, which is weighted toward early time periods. There are gaps in the azimuthal coverage of the storm owing to the small swath width of HIWRAP. These gaps decrease toward the

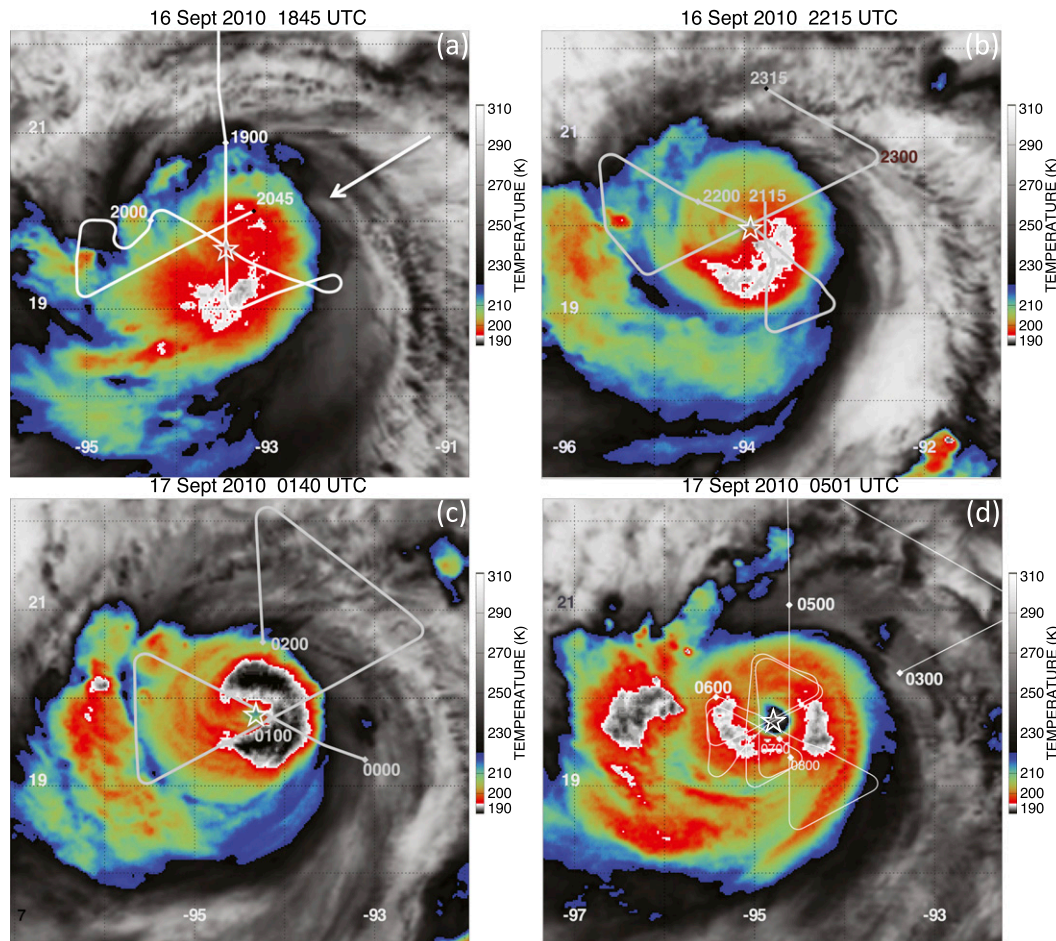


FIG. 2. A sequence of GOES IR images of Hurricane Karl (2010) in the Bay of Campeche during an RI episode spanning the GH flights into the storm. The times shown are (a) 1845 UTC 16 Sep, (b) 2215 UTC 16 Sep, (c) 0140 UTC 17 Sep, and (d) 0501 UTC 17 Sep. The white arrow in (a) denotes the environmental vertical wind shear vector valid over the time interval. The star represents the estimated storm center. The track of the GH  $\pm$  2 h from the satellite time stamp is shown in white with the large numbers denoting the hour (UTC).

storm center where estimates of the low-wavenumber components of the flow are best suited.

Figure 3b shows the horizontal wind speeds at 2-km height averaged over the same time interval. The strongest winds are generally located in the downshear quadrants of the storm with large patches of  $\sim 40$ – $45 \text{ m s}^{-1}$  winds in this region. The time- and azimuthally averaged RMW at this level is 20–25 km. An interesting feature appearing in the data is the presence of small clusters of anomalously large wind speeds located in the eyewall. These clusters have a length scale of  $\sim 10$ – $15 \text{ km}$  and are found most notably in the downshear direction and downshear-left quadrant just inside the RMW.

Figure 4a is similar to Fig. 3a only at 8-km height. At this higher level, the presence of convective burst activity shown by the high reflectivity anomalies between

$\sim 25$  and  $40 \text{ dBZ}$  is evident. These bursts are occurring in the downshear to downshear-left portions of the storm with evidence of rotation into the upshear quadrants observed by tracking the HIWRAP measurements with the GOES IR data. The majority of the burst activity over this time interval is located inside the low-level (2 km) RMW (either time mean or time maximum value), which is consistent with the intensifying TC composite of Rogers et al. (2013). The patches of anomalously large wind speeds shown in Fig. 3b are generally well correlated with the high reflectivity anomalies in Fig. 4a, which suggests the connection of the convective bursts to the localized spinup of the low-level wind field. The association of the high reflectivity anomalies aloft to the localized low-level wind spinup is burdened by the 12–13-h time-averaged perspective. It is also important to keep in mind that



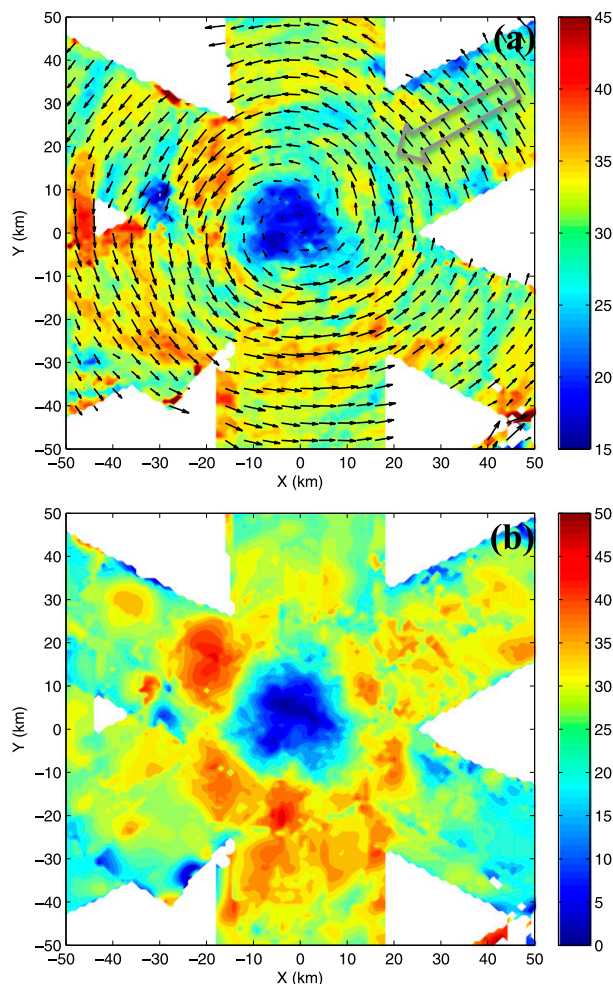


FIG. 3. Composite analysis of HIWRAP data averaged over the total GH sampling interval (12–13 h) at 2-km height for (a) Ku-band reflectivity (dBZ) and horizontal wind vectors and (b) horizontal wind speeds ( $\text{m s}^{-1}$ ). The large gray arrow in (a) is the large-scale vertical wind shear vector valid for this time interval with a value of  $\sim 5 \text{ m s}^{-1}$ .

the number of data points that contribute to the time mean structure in Figs. 3 and 4 are not uniform, especially along the swath edges. Individual overpasses were analyzed and they confirmed the existence of the reflectivity–wind relationship, but uncertainty exists in the timing of the bursts and the anomalously large low-level wind speeds.

Figure 4b shows the horizontal wind speeds at 8-km height, which reveals similar cellular structures as the 2-km wind speeds albeit with generally reduced magnitudes. The strongest wind speeds of  $\sim 35\text{--}40 \text{ m s}^{-1}$  are found in the downshear-left quadrant and the northeast, upshear quadrant at 8-km height. This shows that the enhanced winds associated with the convective bursts extend through a deep layer with the downshear-left

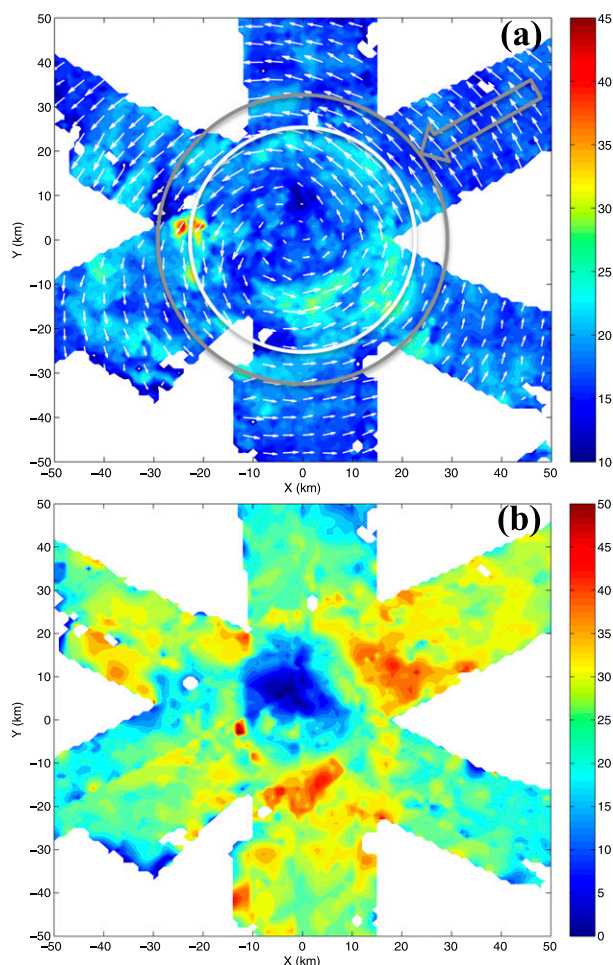


FIG. 4. As in Fig. 3, but for 8-km height. The white circle in (a) shows the location of the low-level (2 km) and time- and azimuthally averaged RMW. The gray circle in (a) shows the maximum azimuthally averaged RMW over the 12–13-h GH sampling period.

quadrant containing the most intense winds. An individual GH overpass in the upshear-left quadrant analyzed later in the paper shows significant tangential wind speeds at upper levels in the convective bursts (Fig. 11d, described in greater detail below), which helps to explain the time-averaged structure in the upshear quadrants shown in Fig. 4b.

The vertical vorticity structure computed from the NOAA TA wind retrievals is shown in Fig. 5 as a prelude to the analysis in the next section. Figure 5a shows the time evolution (1842–2042 UTC 16 September; includes three analysis periods) of the azimuth and height (0.5–4 km) averaged vertical vorticity. At 1842 UTC, the profile of mean vorticity has peak values in the eye and decreases monotonically with radius. At 1930 and 2042 UTC, the peak in mean vorticity moves radially outward to  $\sim 15\text{-km}$  radius (inside the RMW of  $\sim 25 \text{ km}$ )



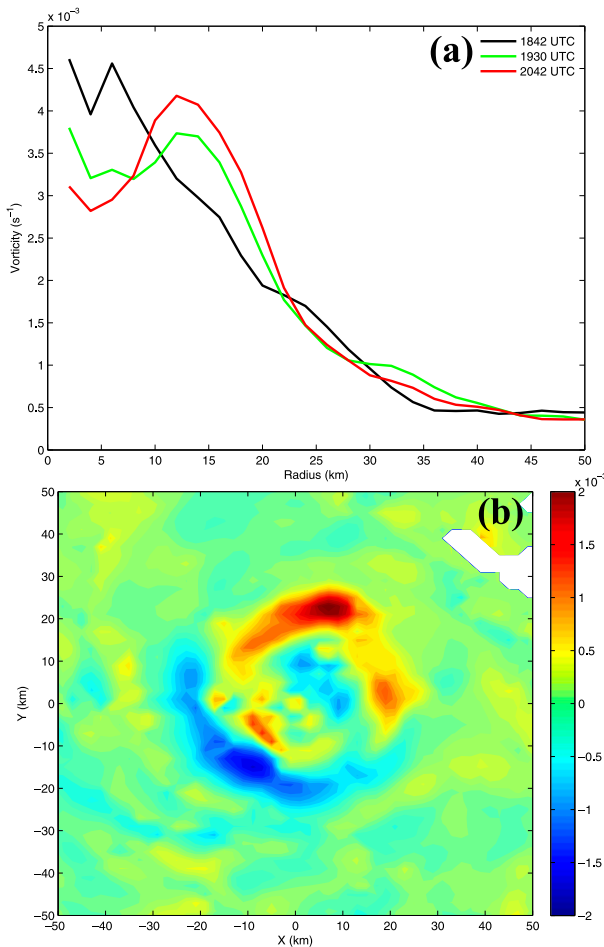


FIG. 5. (a) The vertical vorticity ( $\text{s}^{-1}$ ) computed from NOAA TA wind retrievals averaged between 0.5- and 4-km height and in azimuth for three different time periods. (b) The perturbation vertical vorticity averaged between 0.5- and 4-km height and in time (1842–2042 UTC). The mean RMW during this time period is  $\sim 25$  km.

likely because of the stretching of vorticity from the convective burst activity. The change in sign of the mean radial vorticity gradient at a radius of  $\sim 15$  km for these later periods supports the presence of a vortex-scale instability process likely dominated by barotropic sources (e.g., Schubert et al. 1999; Nolan and Montgomery 2002). However, a more thorough stability analysis is required to determine this conclusively, which is not conducted here.

Kossin and Eastin (2001) analyzed flight-level data in several intense TCs and found similar mean vorticity evolution as that shown in Fig. 5a. They demonstrated that the mixing of vorticity from the eyewall to the eye tended to coincide with the end of intensification. However, the observations presented in this study for Hurricane Karl (2010) indicate that a portion of the

vorticity mixing process is occurring during the RI of the storm.

Figure 5b shows the perturbation (removing azimuthal mean) vorticity averaged over height (0.5–4 km) and time (1842–2042 UTC 16 September) revealing a prominent wavenumber-1 signal driven by vertical wind shear in the eyewall region ( $\sim 20$ – $25$  km) and smaller-scale structure in the eye region. The large oscillations of vorticity observed in the eye region indicate that vorticity has been mixed from the eyewall into the eye region. This mixing and/or transport process could be due to a combination of the vertical-wind-shear-induced asymmetries as well as mesovortices that develop from the breakdown of the vortex instability (e.g., Schubert et al. 1999; Kossin and Eastin 2001). Detailed observations of the convective burst evolution in relation to the inner-core asymmetries are provided in the next section.

### c. Airborne radar and radiometer analysis during the burst pulsing phase

#### 1) FIRST SAMPLING PERIOD ( $\sim 1830$ – $1920$ UTC 16 SEPTEMBER)

The NOAA WP-3D aircraft sampled the RI of Karl at certain similar time periods as the NASA GH, which allows a more comprehensive study of the inner-core processes owing to the large swath width of the WP-3D measurements. The WP-3D first crossed the storm center at  $\sim 1842$  UTC 16 September. The LF radar reflectivity at flight level (3.7-km height) along with the TA radar-derived wind vectors are shown in Fig. 6a at this time.

An interesting wavenumber-5 polygon structure is apparent at the eye–eyewall interface in the LF reflectivity, which is indicative of the presence of mesovortices at the locations of the vertices. The study of Hendricks et al. (2012) observed similar reflectivity structures in the rapid intensification of Hurricane Dolly (2008). The formation of mesovortices has been linked to dynamic instability in the eyewall where thin rings of potential vorticity support the phase locking and exponential growth of counterpropagating vortex Rossby waves (e.g., Schubert et al. 1999; Kossin and Schubert 2001; Rozoff et al. 2009; Hendricks et al. 2014). The above studies showed that the development of mesovortices is an effective means of turbulent mixing between the eye and eyewall, which can lead to important consequences for the intensity of the hurricane. Note that when discussing “turbulent” structures observed in the data presented in this paper, we are referring to azimuthal wavenumbers higher than those associated with mean (wavenumber 0) TC structure.

The wind vectors in Fig. 6a show that the strongest winds ( $\sim 40 \text{ m s}^{-1}$ ) are located in the upshear

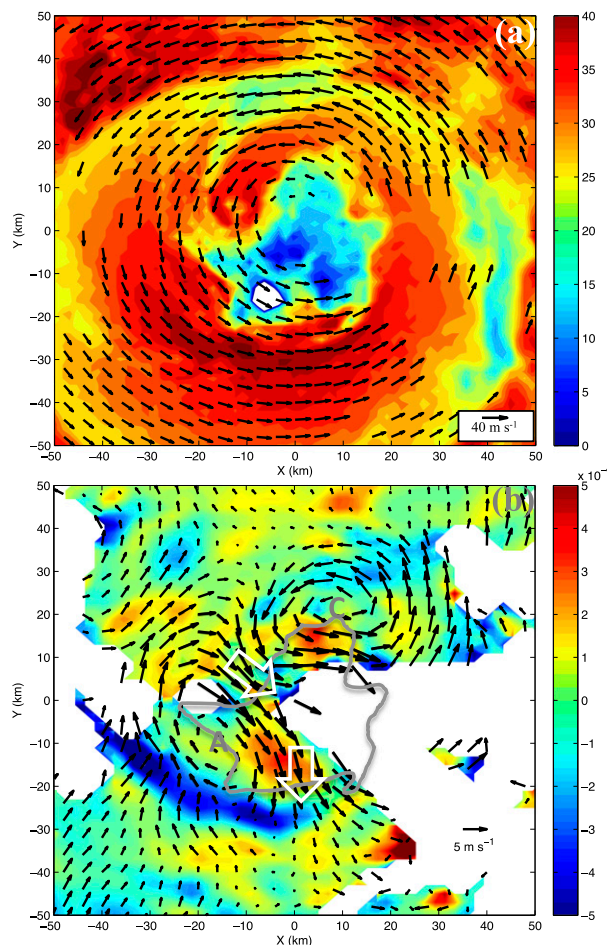


FIG. 6. NOAA WP-3D flight through the inner core of Hurricane Karl (2010) centered at  $\sim 1842$  UTC 16 Sep showing (a) LF C-band reflectivity at 3.7-km height overlaid with TA-derived winds at 4-km height and (b) TA-derived divergence ( $\text{s}^{-1}$ ) averaged between 0.5- and 4-km height overlaid with perturbation wind vectors averaged over the same interval. The white arrows in (b) highlight features discussed in the text. The gray line in (b) marks the eye-eyewall interface using the gradient in LF reflectivity. The gray “C” and “A” letters in (b) denote the centers of cyclonic and anticyclonic mesovortex circulations, respectively.

(northeastern) quadrant at this time and level (4-km height), which is more consistent with the time-averaged HIWRAP data at 8-km height (Fig. 4b) than at 2-km height (Fig. 3b). Figure 6b highlights the 0.5–4-km-height-averaged divergence with perturbation wind vectors (computed by removing the azimuthal mean radial and tangential winds from the total flow and projecting back to Cartesian space) averaged over the same height interval. The analysis in Fig. 6b shows a significant region of outflow emerging from the eye and entering the southern eyewall (see thick arrow in Fig. 6b) where a band of  $\sim 40$ -dBZ echoes are observed (Fig. 6a). A band of strong convergence

extending from the western to southern portions of the eyewall is evident in Fig. 6b, which is consistent with the strongest echoes observed in the LF data (Fig. 6a).

In the northwestern portion of the eyewall, a wide inflow region (see thick arrow in Fig. 6b) with peak magnitudes of  $\sim 8 \text{ m s}^{-1}$  is transporting air across the eye-eyewall interface. The perturbation wind vectors show that a cyclonic-anticyclonic mesovortex couplet is responsible for the transport of air across the eye-eyewall interface on the northwestern side extending down across the southern side. When combined with the vortex-scale inflow (southwestern portion of Fig. 6b radially outside convergence band), the mesovortex-induced outflow across the southern eye-eyewall interface is partly responsible for the convergence band described above. These mesovortices are  $\sim 20$ – $30$  km in spatial scale, which are larger than convective vortices observed previously in TCs (e.g., Reasor et al. 2005; Houze et al. 2009) and in the present paper, which have scales of  $\sim 10$ – $15$  km. We do not observe a wavenumber-5 structure in the perturbation winds as was seen in the LF reflectivity field (Fig. 6a). It is possible that the vortex couplet identified in the wind field is distinct from the structure in the reflectivity field, although data gaps and the relatively coarse resolution of the TA analysis prevent a detailed examination of this linkage.

Figure 7a shows HAMSRS 54-GHz Tbs overlaid with HIWRAP-computed horizontal wind vectors from the first GH overpass of Karl between 1853 and 1919 UTC 16 September. The aircraft crossed the storm center at  $\sim 1910$  UTC, which is  $\sim 25$  min after the WP-3D transect shown in Fig. 6. The data are shown at 2-km height, which is where the HAMSRS 54-GHz weighting function peaks, assuming a standard atmosphere. The presence of light precipitation in the eye of Karl at this time allows the flow in the eye and its interaction with the eyewall to be analyzed.

In this pass, the warm anomaly of Karl is evident shown by the anomalously large Tbs in the core of the storm (5–10 K above ambient values). For this analysis we are not as interested in the quantitative properties of the warm core as our focus is on the qualitative structure of this feature. The eyewall of Karl with embedded convective bursts is seen by the depressed Tbs in the southern half of Fig. 7a with an intense cell located in the eastern half of the southern eyewall, which is in the downshear-left quadrant. The azimuthal mean RMW at this time and height is  $\sim 30$  km, which places the cell inside the RMW. The winds in this region are  $30$ – $40 \text{ m s}^{-1}$  as computed from HIWRAP data.

An interesting feature of the HAMSRS data is a fingerlike protrusion of the warm core sticking out of the southern eyewall and adjacent to the most intense

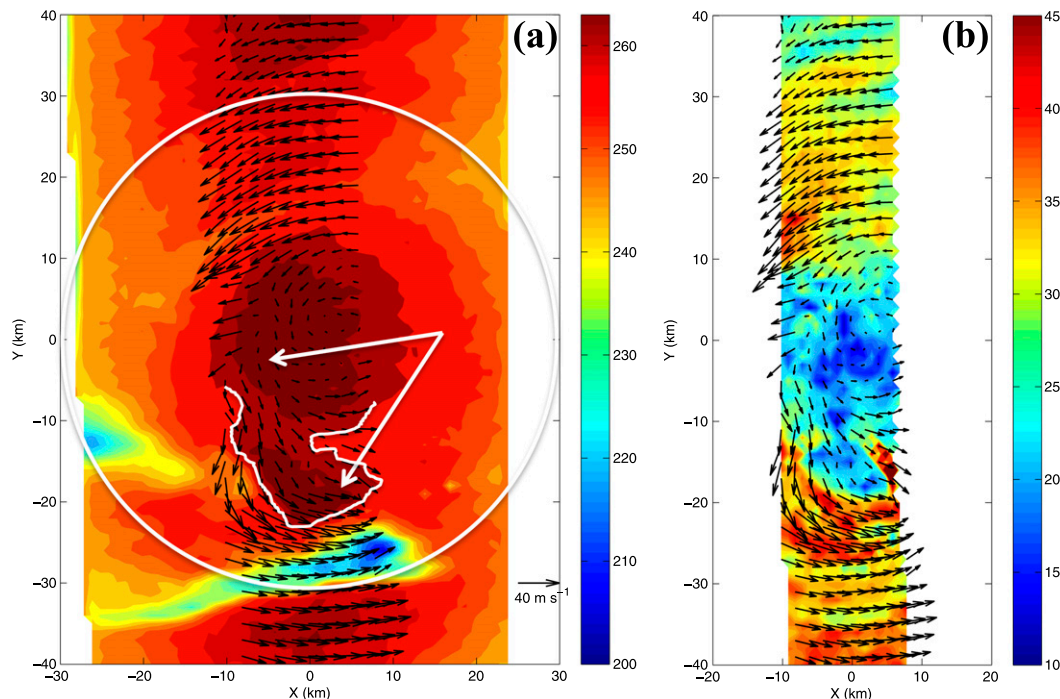


FIG. 7. GH overpass of the inner core of Hurricane Karl (2010) between 1853 and 1919 UTC 16 Sep showing (a) HAMSRS 54-GHz Tbs (K) and (b) HIWRAP Ku-band reflectivity (dBZ). In both panels, horizontal wind vectors from HIWRAP are overlaid and the analysis level is 2-km height. The white arrows and white outline in (a) highlight a protrusion of the warm core discussed in the text. The azimuthal mean RMW at 2-km height of  $\sim 30$  km is also shown in (a) by the white circle. The reference wind vector in (a) applies to both panels.

convective activity (labeled with white in Fig. 7a). The HIWRAP winds follow this feature well and show  $10\text{--}20\text{ m s}^{-1}$  flow originating in the eye and cyclonically rotating toward the intense convective cell in the eastern half of the southern eyewall. The winds from this warm anomaly protrusion show a convergence signature with the intense convective cell.

Figure 7b (also at 2-km height) shows Ku-band reflectivity from HIWRAP along with horizontal wind vectors for the same overpass as in Fig. 7a. The warm core protrusion observed in the HAMSRS data can also be seen in the HIWRAP data through reduced reflectivity in the southern eye/eyewall from values of  $35\text{--}40$  to  $\sim 20$  dBZ. The analysis above indicates that turbulent mixing between the warm, dry air in the eye with moist air in the eyewall is helping to carve out and develop the eye of Karl. Reducing the reflectivity through mixing and evaporation should help ensuing subsidence to go more directly into warming the eye. This is a general statement not specifically targeted at the structure shown in this overpass. While axisymmetric warming of the eye from the vortex response to convective heating is likely significant in the RI of Karl (e.g., Vigh and Schubert 2009), the asymmetric mixing process described above can certainly assist the total

development of the eye and warm core. Note that HAMSRS and HIWRAP data at 1-, 3-, and 4-km height showed very similar structure to that illustrated in Fig. 7 at 2-km height.

In addition to the HIWRAP winds in Fig. 7, the LF reflectivity structure (Fig. 6a) and TA perturbation winds (Fig. 6b) observed  $\sim 25$  min earlier show that the turbulent mixing is a result of mesovortices located near the eye–eyewall interface (also see discussion in section 4b). Small patches of reduced reflectivity (Fig. 7b) in the same locations as the low Tbs in Fig. 7a are the result of attenuation of the HIWRAP Ku-band signal from the convective bursts.

Figure 8 shows nadir cross sections of HIWRAP data for the first GH overpass (see Fig. 7). This cross section is straight through the storm center in the north-to-south direction. Figure 8a shows Ku-band reflectivity through the convective burst in the southern eyewall revealing a deep column of high values reaching  $\sim 35$  dBZ at 12-km height ( $x$  axis =  $\sim -25$  km). There is a large region of lower reflectivity ( $\sim 20$  dBZ) filling the eye that is connected with the convective burst in the southern eyewall at  $x$  axis =  $\sim -20$  km,  $y$  axis =  $\sim -8$  km. In the eye region, there is a deep layer (1–10 km) of outflow with peak magnitudes from  $\sim -10$  to  $-15\text{ m s}^{-1}$  (Fig. 8b,



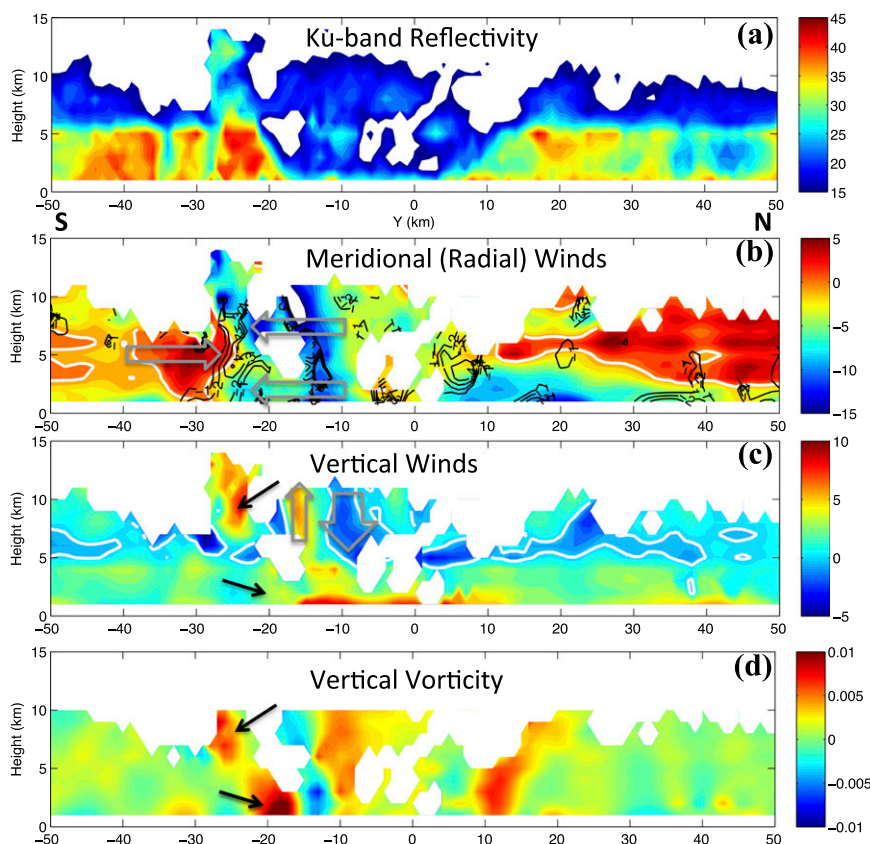


FIG. 8. HIWRAP vertical cross sections at nadir through the storm center in the north-to-south direction for the GH overpass between 1853 and 1919 UTC 16 Sep. The data shown are (a) Ku-band reflectivity (dBZ), (b) meridional (radial) winds ( $\text{m s}^{-1}$ ) with divergence overlaid in black contours (values shown are from  $-4 \times 10^{-3}$  to  $-1 \times 10^{-3} \text{ s}^{-1}$ ), (c) vertical winds ( $\text{m s}^{-1}$ ), and (d) vertical vorticity ( $\text{s}^{-1}$ ). The large gray arrows in (b),(c) highlight features discussed in the text while the white lines in these panels show the zero contours. The black arrows in (c),(d) also highlight features discussed in the text. Note the azimuthal mean RMW at 2-km height at this time is  $\sim 30$  km.

$x$  axis =  $\sim -15$  km), which is consistent with the warm core mixing into the eyewall shown in Fig. 7a at 2-km height. The outflow from the eye converges with inflowing air, located radially outside the convection, at low to midlevels in the core of the burst (see divergence contours and gray arrows in Fig. 8b).

These data indicate that the maintenance of the convective burst in the southern eyewall (downshear-left quadrant) is driven by a combination of buoyancy (inferred from Fig. 7a) and horizontal, kinematic convergence (Fig. 8b). Both of these mechanisms are facilitated by the turbulent mixing of air, originating in the anomalously warm eye, with inflowing air in the low-to-midlevel eyewall. During this first sampling period it was difficult to determine if the convective burst was in the formation stage or a mature stage and, thus, the mechanisms outlined above more directly point to maintenance of the burst. However, similar mechanisms were

operating during the third sampling period where observations more clearly show the burst formation stage.

A significant region of descent with peak values of  $\sim -3 \text{ m s}^{-1}$  is located in the eye of Karl (wide gray arrow in Fig. 8c), which should be helping to clear and warm the eye. This descent appears to be induced by the convective updraft (thin gray arrow in Fig. 8c) occurring on the inner edge of the eyewall ( $x$  axis =  $\sim -15$  km). There is also a downdraft located radially inward of the convective burst ( $x$  axis =  $\sim -18$  km,  $y$  axis =  $\sim 7$ – $10$ -km height), which is also well positioned to warm and dry the eye. The convectively induced downdrafts observed in this overpass are consistent with prior airborne Doppler radar studies of TCs (Heymsfield et al. 2001; Guimond et al. 2010).

A reasonably strong updraft of  $\sim 10 \text{ m s}^{-1}$  (Fig. 8c) in the core of the deep convection ( $x$  axis =  $\sim -25$  km) is nearly coincident with an anomalously large patch of



cyclonic vorticity (Fig. 8d) at  $\sim 7$ -km height (denoted with black arrow). Note that vorticity values are removed above 10-km height because the swath width of the HIWRAP data at these levels is very small, which places the swath edges close to nadir. The computed horizontal winds at the swath edges have larger uncertainty owing to the HIWRAP scanning geometry (Guimond et al. 2014). At low levels on the inner edge of the deep convection ( $x$  axis =  $\sim -18$  km), a weak-moderate updraft of  $\sim 3\text{--}5\text{ m s}^{-1}$  (Fig. 8c) is collocated with an intense cyclonic vorticity anomaly with values of  $10^{-2}\text{ s}^{-1}$  (Fig. 8d). Note that the main updraft for the convective burst may be sloped such that the vertical cross sections in Figs. 8c and 8d may not have perfectly correlated vertical velocity and vertical vorticity structure in the vertical plane. These observations suggest that the convective burst sampled here is rapidly rotating through a deep layer as has been observed in previous studies (e.g., Reasor et al. 2005; Houze et al. 2009).

## 2) SECOND SAMPLING PERIOD ( $\sim 1920\text{--}2000$ UTC 16 SEPTEMBER)

Approximately 20 min after the first GH overpass, the NOAA WP-3D aircraft penetrated the core of Karl again with a center crossing at  $\sim 1930$  UTC 16 September. Figure 9a shows LF radar reflectivity at flight level (3.6-km height) along with the TA radar-derived wind vectors at 4-km height. Intense reflectivity between 45 and 50 dBZ is present on the western half of the storm while the eastern half is ragged without a continuous region of elevated reflectivity. Significant reflectivity is located in the eye of the storm and animations of several LF scans show mesovortex-like features mixing into the eye from the eyewall. Much like the previous transect, the strongest winds are located in the northeastern (upshear) quadrant.

Figure 9b shows the perturbation wind vectors, averaged over the 0.5–4-km height interval, overlaid on the mean divergence field in this same layer. Note that individual levels at 0.5 and 1 km showed very similar structure to the layer mean. A region of strong convergence is located in the western eyewall, which appears to extend down to the southwestern eyewall similar to Fig. 6b, but the data gaps prevent a clear analysis. The convergence region in the western eyewall (downshear quadrants) is consistent with the intense reflectivity band (Fig. 9a), while the eastern eyewall (upshear quadrants) is having difficulty developing perhaps as a result of the vertical wind shear.

The perturbation wind vectors in Fig. 9b reveal a similar cyclonic–anticyclonic mesovortex couplet as the previous transect (Fig. 6b) although a data gap in the southwestern quadrant makes the placement of the

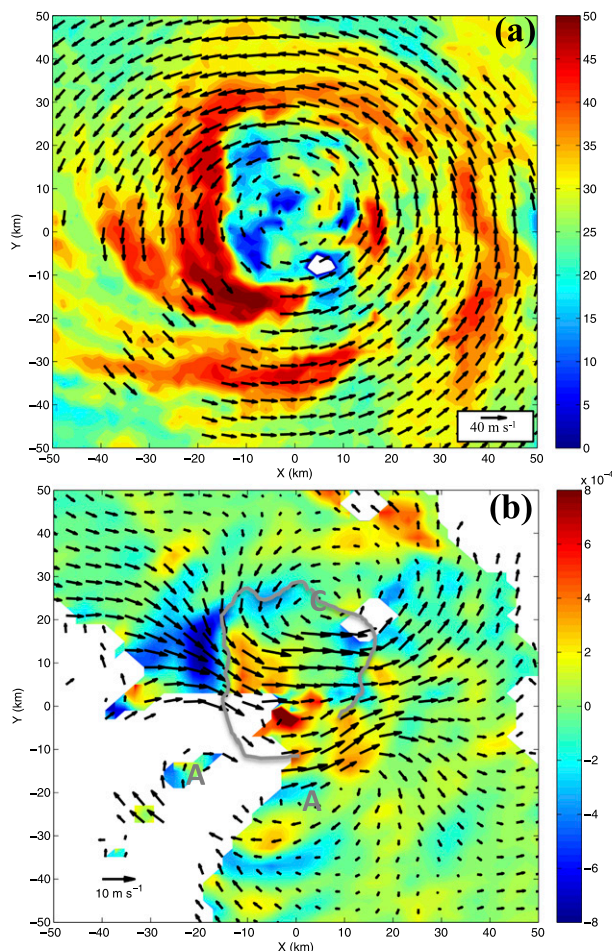


FIG. 9. NOAA WP-3D flight through the inner core of Hurricane Karl (2010) centered at  $\sim 1930$  UTC 16 Sep showing (a) LF reflectivity at 3.6-km height overlaid with TA-derived winds at 4-km height and (b) TA-derived divergence ( $\text{s}^{-1}$ ) averaged between 0.5- and 4-km height overlaid with perturbation wind vectors averaged over the same interval. The gray line in (b) marks the eye-eyewall interface using the gradient in LF reflectivity. The gray “C” and “A” letters in (b) denote the centers of cyclonic and anticyclonic mesovortex circulations, respectively.

anticyclonic circulation rather broad and with some uncertainty. Nevertheless, the counterrotating circulations are consistent with the convergence signature in the western eyewall. The cyclonic circulation at the northern eye-eyewall interface is meeting inflowing air in the northwestern portion of Fig. 9b as well as the flow associated with the anticyclonic mesovortex in the southwestern eyewall region. These mesovortex circulations are consistent with the wavenumber-1 structure in the vorticity field (Fig. 5b) and are directing air across the eye-eyewall interface with inflow to the eye on the western side and outflow to the eyewall on the eastern side.

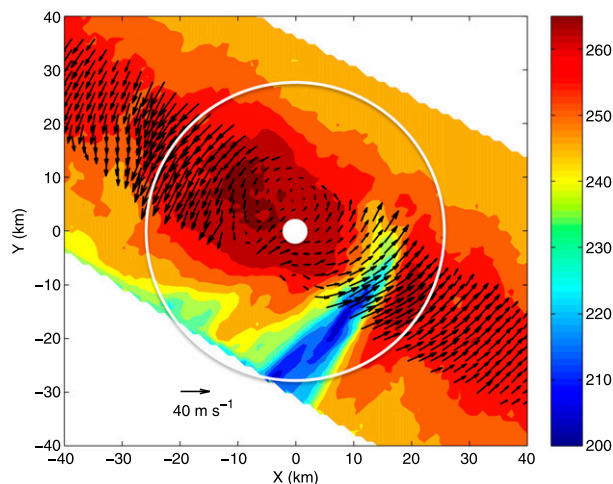


FIG. 10. As in Fig. 7a, but for the GH overpass between 1938 and 1957 UTC 16 Sep. The large white circle denotes the azimuthally averaged RMW at 2-km height of  $\sim 25$  km and the white dot is the storm center.

Figure 10 is similar to Fig. 7a only for the second GH overpass of Karl between 1938 and 1957 UTC 16 September. This is a diagonal pass from southeast to northwest, which covers part of the upshear-left quadrant of the storm where depressed Tbs from HAMSR show the straining/elongation of deep convection by the advective tendencies of the cyclonic flow. The maximum HIWRAP winds at 2-km height are  $\sim 50 \text{ m s}^{-1}$  in the northwestern eyewall and  $\sim 30 \text{ m s}^{-1}$  in the southeastern eyewall where the flow has a radially outward directed component into the convection. The warmest Tbs are located on the northwestern side of the eye.

The vertical structure of HIWRAP Ku-band reflectivity at nadir for this overpass is shown in Fig. 11a. Deep convection with similar vertical structure to that shown in the previous GH overpass (Fig. 8a) is observed in the southeastern (upshear left) portion of the eyewall with significant reflectivity filling the eye adjacent to this cell. The northwestern portion of the eyewall is not as convectively active and the eye is clear adjacent to this side of the eyewall, which is consistent with the previous overpass and the warmest Tbs shown in Fig. 10. The RMW at 2-km height for this sampling period is 26 km, which is  $\sim 3$  km smaller than the first sampling period. In both periods, the convective bursts are located just inside the RMW, which is consistent with the RI of Karl and a contracting eyewall.

Figure 11b shows the radial wind speeds for this overpass. The dominant features are a region of mid-level inflow located radially outside the convective burst and a deep column of strong outflow that traverses the

eye region and enters the core of the burst (see gray arrows). The flow across the eye is similar to that observed by the WP-3D shown in Fig. 9b and is driven by the counterrotating mesovortex circulations. These winds acquire entropy from the warm anomaly eye (see Fig. 10) likely leading to assistance in convective development in the southeastern eyewall through buoyancy effects. Regions of convergence at low and midlevels (Fig. 11b) are located on the outer edge of the burst ( $x$  axis from  $\sim -20$  to  $-30$  km). Also note in Fig. 11b that the outflow at low levels on the southeastern side (upshear left) and the inflow on the northwestern side (downshear right) is indicative of the shear-induced anomalies to the secondary circulation shown in Reasor et al. (2013).

The vertical motion structure in Fig. 11c shows a broad region of descent in the eye adjacent to the convective burst with values from  $\sim -2$  to  $-4 \text{ m s}^{-1}$ . This descent appears to be generated by the convective activity through compensating motions around convective updrafts (see gray arrows). The broad region of forced descent in the eye is similar to that observed in the previous overpass in the downshear-left quadrant. This robust structure should lead to a drying and warming effect over time, which will be demonstrated with the data in subsequent overpasses.

Finally, instead of showing the vorticity for this overpass, which was somewhat similar to the previous transect, the tangential winds are presented in Fig. 11d. The tangential winds are  $\sim 20 \text{ m s}^{-1}$  stronger in the northwestern eyewall up to midlevel regions with peak values of  $\sim 50 \text{ m s}^{-1}$  at low levels. In the deep convection, large tangential wind speeds are located at high levels (12–13 km), which is due to strong updrafts transporting high angular momentum air aloft. It appears the convective towers are trying to build a deeper, more intense vortex in this portion of the eyewall.

### 3) THIRD SAMPLING PERIOD ( $\sim 2030$ – $2100$ UTC 16 SEPTEMBER)

The NOAA WP-3D tracked through the center of Karl one last time centered at 2042 UTC 16 September. Figure 12 shows four LF reflectivity snapshots covering a 2.5-min period between 2039:40 and 2042:13 UTC. These images show that the western/northwestern eyewall with embedded deep convective towers is intensifying rapidly (in terms of reflectivity) during this 2.5-min time period. A cyclonic mesovortex identified in the HIWRAP and TA wind fields during this time period (next two figures) is located at the eye–eyewall interface adjacent to this convective burst development.

Figure 13a shows the LF reflectivity at flight level (3.6 km) along with TA-derived wind vectors at 4-km

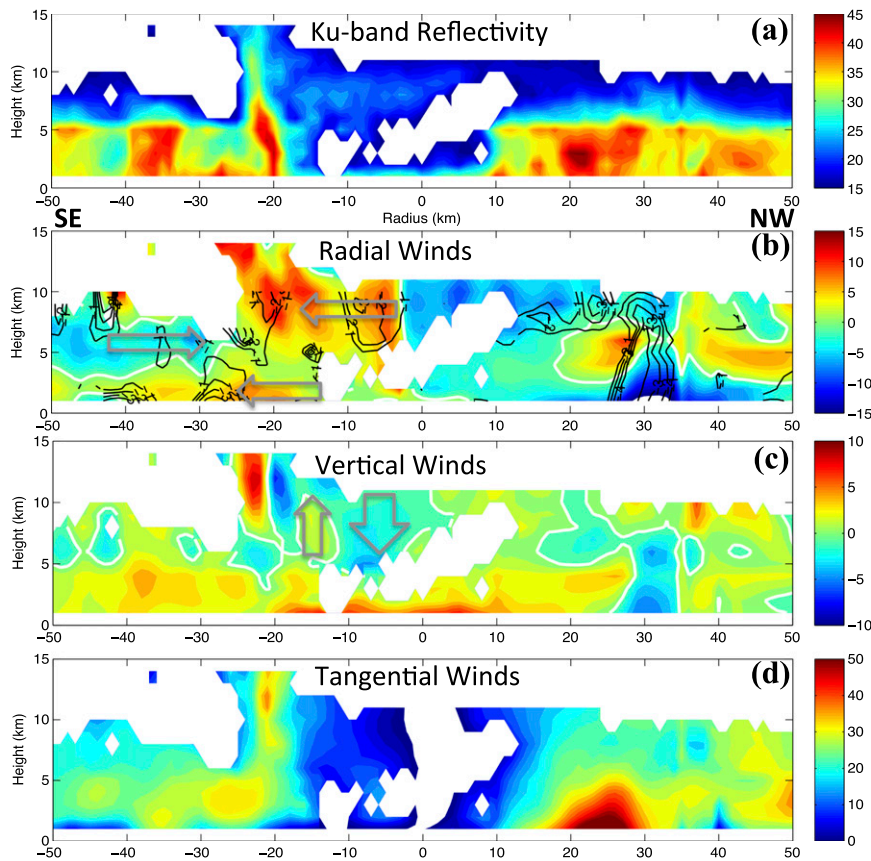


FIG. 11. As in Fig. 8, but for the GH overpass between 1938 and 1957 UTC 16 Sep in the southeast (negative radius) to northwest (positive radius) direction. The data shown are (a) Ku-band reflectivity (dBZ), (b) radial winds ( $\text{m s}^{-1}$ ) with divergence overlaid in black contours (values shown are from  $-4 \times 10^{-3}$  to  $-1 \times 10^{-3} \text{ s}^{-1}$ ), (c) vertical winds ( $\text{m s}^{-1}$ ), and (d) tangential winds ( $\text{m s}^{-1}$ ). The gray arrows in (b),(c) highlight features discussed in the text while the white lines in these panels show the zero contours. Note the azimuthal mean RMW at 2-km height at this time is  $\sim 25$  km.

height and 2042:13 UTC. The western eyewall is the dominant feature with a large region of reflectivity at or above 50 dBZ. The horizontal winds in this region are  $\sim 10 \text{ m s}^{-1}$  stronger than those from the previous WP-3D sampling  $\sim 1$  h earlier at 1930 UTC (see Fig. 9a). The eastern eyewall is still ragged without a coherent eyewall apparent in the reflectivity, while the southern eyewall has increased banding features, which appear to be coalescing.

The divergence field for this flight averaged over the 0.5–4-km layer is shown in Fig. 13b with 0.5–4-km-height-averaged perturbation winds overlaid. The cyclonic–anticyclonic mesovortex couplet identified in the previous WP-3D penetrations continues to persist two hours after initial diagnosis. At this time period, the mesovortex couplet has rotated cyclonically with the mean flow placing the cyclonic circulation directly north of the anticyclonic circulation in the western eyewall.

These circulations are consistent with a strong region of convergence in the western eyewall (similar to previous transect in Fig. 9b), which is helping to trigger the convective bursts, and a west-to-east flow across the eye. In the eastern eyewall, which is not well defined in the LF reflectivity, another small-scale cyclonic circulation is evident in the perturbation wind vectors. This circulation is helping to direct a southerly flow across portions of the eastern eye–eyewall interface.

The next GH overpass of Karl sampled directly along the shear vector with a southwest-to-northeast transect just north of the storm center at  $\sim 2040$  UTC 16 September, which is  $\sim 2$  min behind the WP-3D. Figure 14 shows HAMS 54-GHz Tbs along with HIWRAP horizontal wind vectors at 2-km height for this overpass. A very intense convective cell located in the downshear direction is present in the HAMS data with Tbs falling well below 200 K (strong ice scattering) in the



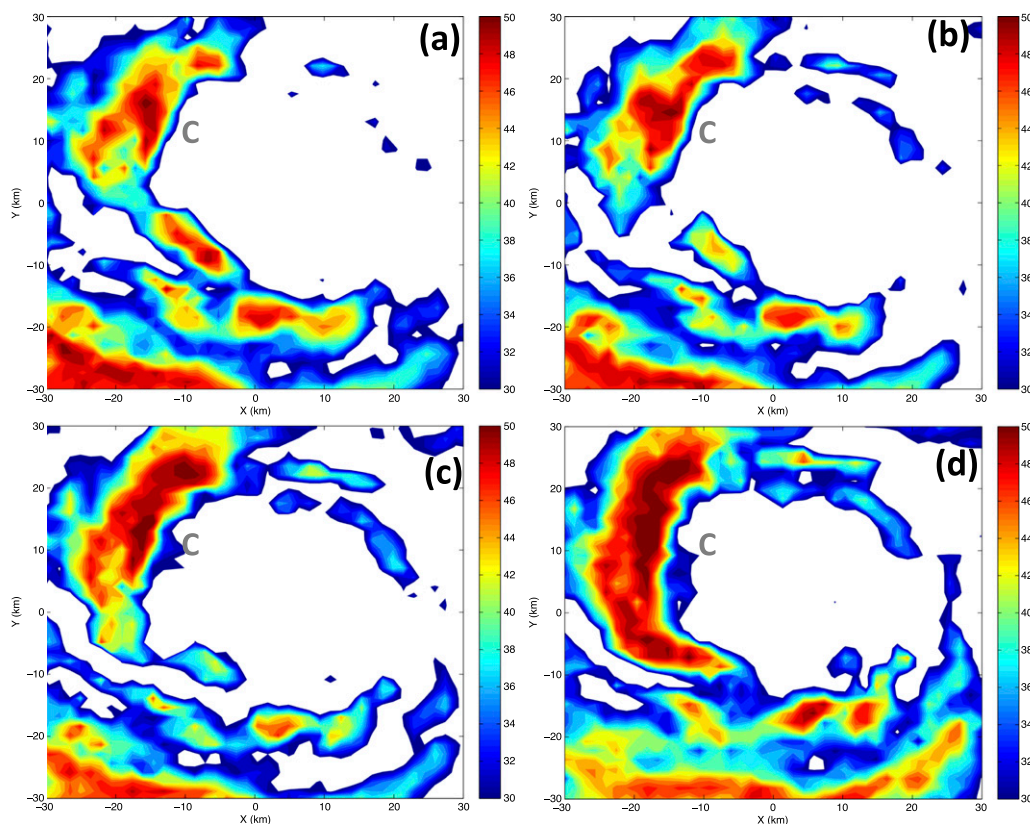


FIG. 12. Snapshots of LF reflectivity at 3.6-km height covering a 2.5-min period between 2039:40 and 2042:13 UTC 16 Sep. The times shown are (a) 2039:40, (b) 2040:10, (c) 2040:42, and (d) 2042:13 UTC. The gray “C” letter in each panel denotes the center of a cyclonic mesovortex circulation identified in HIWRAP and TA wind fields during this time period (see Figs. 13b and 14).

core of the  $\sim 10$ -km-wide feature. This cell is located at and just inside the azimuthally averaged RMW at this level.

In the eye of the storm, the HIWRAP winds reveal a cyclonic mesovortex circulation that is directing air out of the northern portion of the eye and into the convective burst. The HAMS data show that the air being transported into the burst is anomalously warm with Tbs significantly larger than ambient values. The mesovortex circulation identified in the HIWRAP data is also seen at the same location in the TA perturbation wind vectors (see Fig. 13b).

The close coordination of the GH and WP-3D aircraft during this time allows a comparison of the storm kinematic structure from the HIWRAP and TA radars. The appendix also shows error statistics between HIWRAP-computed winds and WP-3D flight-level data.

Figure 15a shows HIWRAP Ku-band reflectivity in a vertical cross section averaged between  $\sim 0$  and 6 km in the  $+y$  direction (see Fig. 14 for averaging domain). HIWRAP shows an intense convective cell with elevated reflectivity to  $\sim 15$ -km height in the downshear eyewall of Karl. The WP-3D reflectivity (not shown)

shows similar features albeit with a more diffuse cell. The radial winds from HIWRAP (Fig. 15b) show a strong convergence signature directly below the intense convective cell with outflow of  $\sim 5\text{--}8\text{ m s}^{-1}$  crossing the eye-eyewall interface. This outflow from the eye brings warm anomaly air into the eyewall helping to fuel the developing convective cell (see also Figs. 7 and 14). The location of the low-level convergence signature inside the RMW shown in Fig. 15b is consistent with the study of Rogers et al. (2015) for the RI of Hurricane Earl (2010).

A deep column (1–12 km) of inflow (from  $\sim -5$  to  $-10\text{ m s}^{-1}$ ) coincident with the convective cell is present in the HIWRAP data (Fig. 15b) and in the TA data at low and high levels (Fig. 15c), which acts to locally spin up the tangential winds through the inward transport of high angular momentum air. The TA-derived radial winds in Fig. 15c show similar features in similar locations to the HIWRAP fields in Fig. 15b, but the intensity of the flow is somewhat reduced in the TA fields.

The HIWRAP-derived vertical winds (Fig. 15d) show a deep updraft is present in the core of the



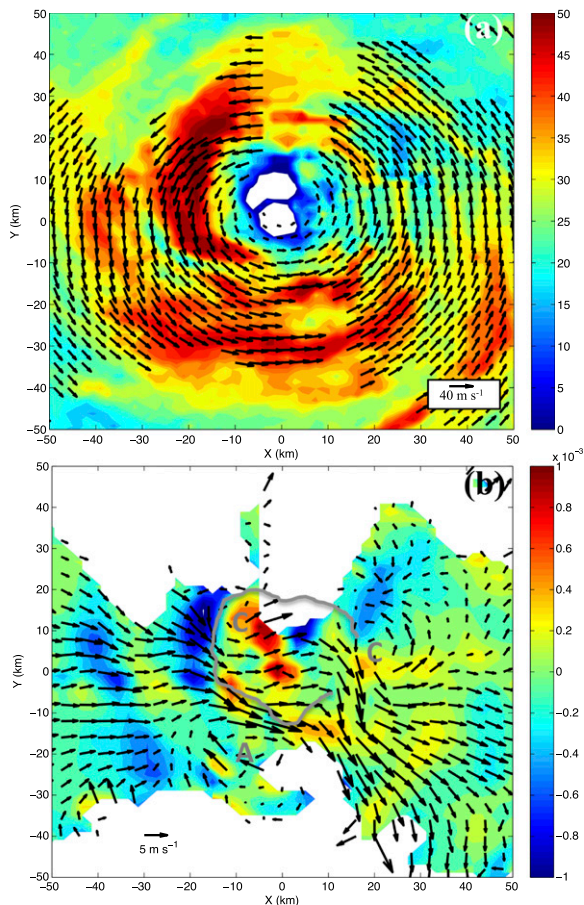


FIG. 13. As in Fig. 9, but for the NOAA WP-3D transect centered at  $\sim 2042$  UTC 16 Sep.

convective cell with a strong pulse approaching  $10 \text{ m s}^{-1}$  located at  $\sim 10$ -km height. A downdraft of from  $\sim -3$  to  $-5 \text{ m s}^{-1}$  is located on the inner edge of the eyewall (see gray arrow), which is likely formed through mass conserving motions around the strong updraft. The TA-derived vertical winds in Fig. 15e show similar structures to those from HIWRAP but, again, with reduced magnitudes. The TA data in Fig. 15e also show compensating downdrafts on either side of the updraft with a broad region of descent (from  $\sim -1$  to  $-2 \text{ m s}^{-1}$ ) located radially inward of the cell (see gray arrow). This broad descent is well positioned to dry and warm the eye as observed in previous overpasses (see Fig. 8c and Fig. 11c) and is a common feature around convective towers located in the eyewall of intensifying TCs (e.g., Heymsfield et al. 2001; Guimond et al. 2010).

The generally favorable comparisons between the HIWRAP- and TA-derived winds shown in Fig. 15 (as well as the comparisons in the appendix) provide confidence in the HIWRAP data and retrievals shown in this paper, which are not as mature as the TA fields. The

reduced wind magnitudes in the TA data were found to be largely a result of a Gaussian distance-weighted interpolation used in the TA wind retrieval [see appendix of Reasor et al. (2009)]. A higher-resolution TA product that minimizes smoothing was also analyzed and showed increased wind magnitudes more similar to HIWRAP. These comparisons are not shown for brevity and because this product was only available along the aircraft track.

#### d. HIWRAP data analysis during the vortex response phase

The main advantage of the GH aircraft is the long duration sampling, which allows continued analysis of the RI of Karl when the WP-3D aircraft returned to base following the 2042 UTC 16 September eye penetration. The GOES IR satellite data analyzed in section 4a showed that the majority of the convective burst activity was finished by  $\sim 0000$  UTC 17 September. After this time, the vortex went through a response phase that included axisymmetrization of the convective anomalies, which was sampled by the GH aircraft for a period of  $\sim 8$  h.

Figure 16 shows vertical cross sections of HIWRAP Ku-band reflectivity and tangential wind speed at nadir for a series of overpasses of the inner core of Karl spanning this 8-h period. At 0012 UTC 17 September (Fig. 16a), the vertical structure of the eye/eyewall already looks different than that shown for the burst pulsing phase (e.g., Fig. 8a and Fig. 11a). There is little reflectivity filling the eye, and the beginning of a more sloped structure to the eyewall is observed. The tangential winds peak at  $\sim 40 \text{ m s}^{-1}$  in the southeastern quadrant and  $\sim 45 \text{ m s}^{-1}$  in the northwestern quadrant with both sides showing contours sloping outward with height. About 3.5 h later at 0345 UTC (Fig. 16b), the axisymmetric structure reflected in the cross section continues to develop with significant sloping of the eyewall reflectivity and tangential winds with height. The eye has also widened, which is indicative of increased subsidence and growth of the warm core (backed by HAMS data; not shown) in association with an enhanced secondary circulation from the vortex response to the convective forcing.

Over the next  $\sim 4$  h, the trend toward a wider, clearer, and warmer eye with a sloping eyewall structure reminiscent of axisymmetric hurricanes continues to prevail (Figs. 16c,d), except for the presence of a transient convective burst in the northwestern eyewall in Fig. 16c.

## 5. Summary and conclusions

In this paper, the evolution of rapidly intensifying Hurricane Karl (2010) is examined from a suite of

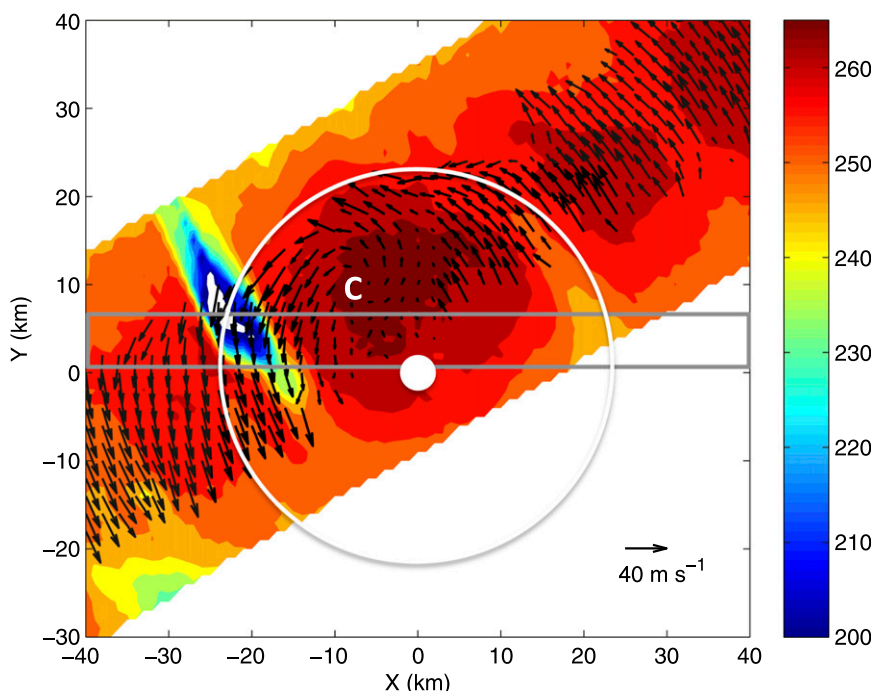


FIG. 14. As in Fig. 7a, but for the GH overpass between 2009 and 2055 UTC 16 Sep with a center crossing at  $\sim 2040$  UTC. The large white circle denotes the azimuthally averaged RMW at 2-km height and the white dot is the storm center. The gray box shows the region where data are averaged in the  $y$  direction for subsequent figures. The “C” letter denotes the center of a mesovortex cyclonic circulation.

remote sensing observations during the NASA Genesis and Rapid Intensification Processes (GRIP) field experiment. The novelties of this study are in the analysis of data from a new airborne Doppler radar (HIWRAP) and a new airborne platform (NASA Global Hawk) for hurricane research that allows long endurance sampling (up to 24 h). Supporting data from a microwave sounder (HAMSR) coincident with HIWRAP and coordinated flights with the NOAA WP-3D aircraft carrying the lower fuselage (LF) and tail (TA) radars help to provide a detailed analysis of the storm. The focus of the analysis is on documenting and understanding the structure, evolution, and role of small-scale, deep convective forcing in the storm intensification process.

After Karl emerged off the Yucatan Peninsula as a tropical storm, satellite data revealed the presence of deep convective bursts located primarily in the downshear to downshear-left quadrants of the storm. The bursts went through a  $\sim 12$ -h pulsing phase followed by a vortex response phase that included axisymmetrization of the convective anomalies and the development of a wide, clear eye. During this evolution, the surface wind speeds in Karl increased by  $\sim 37 \text{ m s}^{-1}$  in a 30-h period, which is more than double the typical rapid intensification rate of  $\sim 15 \text{ m s}^{-1}$  in 24 h (Stewart 2011).

The Global Hawk (GH) and WP-3D aircraft data were analyzed from  $\sim 1900$  UTC 16 September to 0800 UTC 17 September, which covered portions of the convective burst pulsing phase and vortex response phase. The aircraft remote sensing data and analysis indicate the following science results.

The convective bursts formed primarily in the downshear to downshear-left quadrants through a combination of two main processes: 1) convergence generated from counterrotating mesovortex circulations and the larger vortex-scale flow and 2) the turbulent (scales of  $\sim 25$  km) transport of anomalously warm, buoyant air from the eye to the eyewall at low levels. Calculations of dynamical fields such as vorticity from the TA wind analyses showed the presence of a deep (0.5–4-km height) and persistent (at least 2 h) wavenumber-1 mode at the eye–eyewall interface during the burst pulsing phase consistent with the mesovortex circulations.

Reflectivity snapshots and animations from the LF radar showed a distinct wavenumber-5 structure at the eye–eyewall interface in one WP-3D transect of the storm and the movement of small-scale features in the eye and across the interface during the aircraft-sampling period. These structures and the observed turbulent

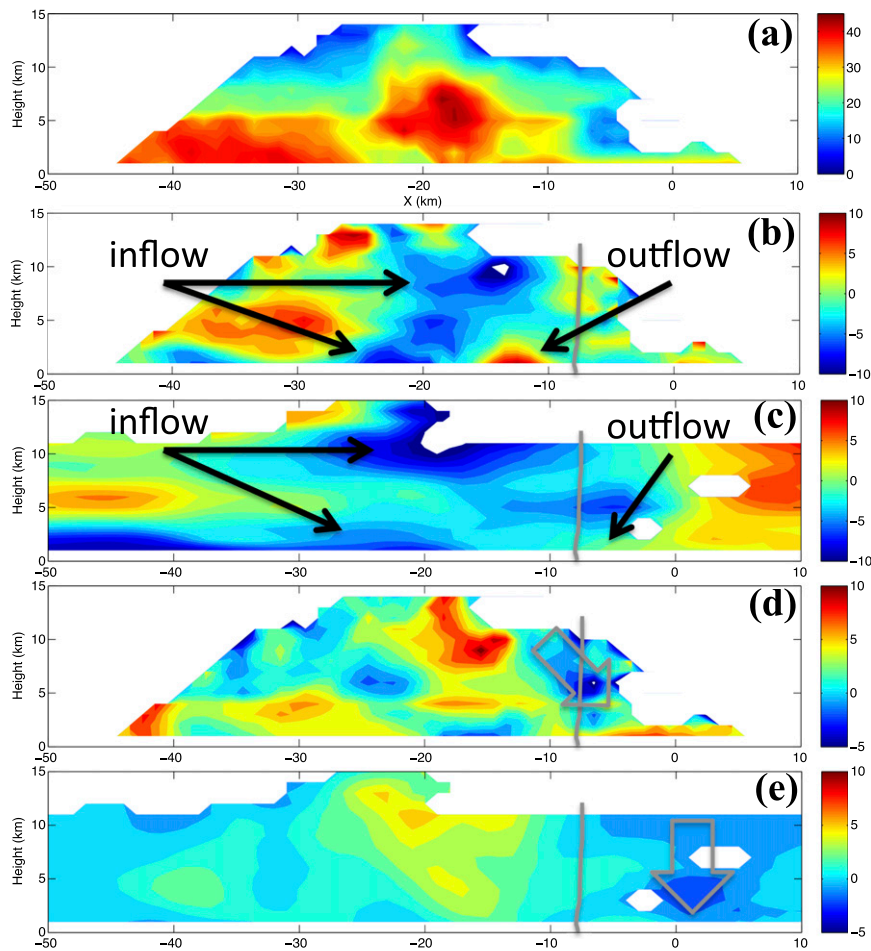


FIG. 15. Vertical cross sections of radar data averaged between  $\sim 0$  and 6 km in the  $+y$  direction (see Fig. 14) from (a) HIWRAP Ku-band reflectivity (dBZ) valid at  $\sim 2040$  UTC 16 Sep, (b) HIWRAP-derived radial winds ( $\text{m s}^{-1}$ ), (c) NOAA WP-3D-derived radial winds ( $\text{m s}^{-1}$ ) valid at  $\sim 2042$  UTC 16 Sep, (d) HIWRAP-derived vertical winds ( $\text{m s}^{-1}$ ), and (e) NOAA WP-3D-derived vertical winds ( $\text{m s}^{-1}$ ). Note that there are no data on the right side of the HIWRAP panels owing to the coverage and cross section cut. The vertical gray line in (b)–(e) denotes the western eye–eyewall interface using the gradient in reflectivity. The large gray arrows in (d), (e) highlight features discussed in the text.

mesovortex circulations that produce significant eye–eyewall mixing likely form as a result of the vertical wind shear forcing and dynamic instability in the axisymmetric vortex (e.g., Schubert et al. 1999; Kossin and Schubert 2001; Rozoff et al. 2009; Hendricks et al. 2012), which was shown to be present during the rapid intensification of Karl.

Horizontal wind fields computed from the TA and HIWRAP measurements showed that the mesovortex circulations were primarily located in the western and southern (downshear) eye/eyewall region where the most intense convective activity was found. In one GH overpass, a fingerlike protrusion of the warm core observed from HAMSAR was observed to rotate

cyclonically into the eyewall, likely helping to fuel convective towers observed in this region. Figure 17 shows a conceptual diagram summarizing the remote sensing measurements and the analysis of the mesoscale dynamics described above. Each physical process highlighted in the conceptual diagram can be traced back to specific figures shown in the paper. For example, the cyclonic rotation of warm air from the eye to the eyewall in the downshear-left portion of Fig. 17 is related to Fig. 7a.

The mechanism for convective burst formation identified in the observations is similar to that determined by Braun et al. (2006) using a numerical simulation of Hurricane Bonnie (1998). In this study,



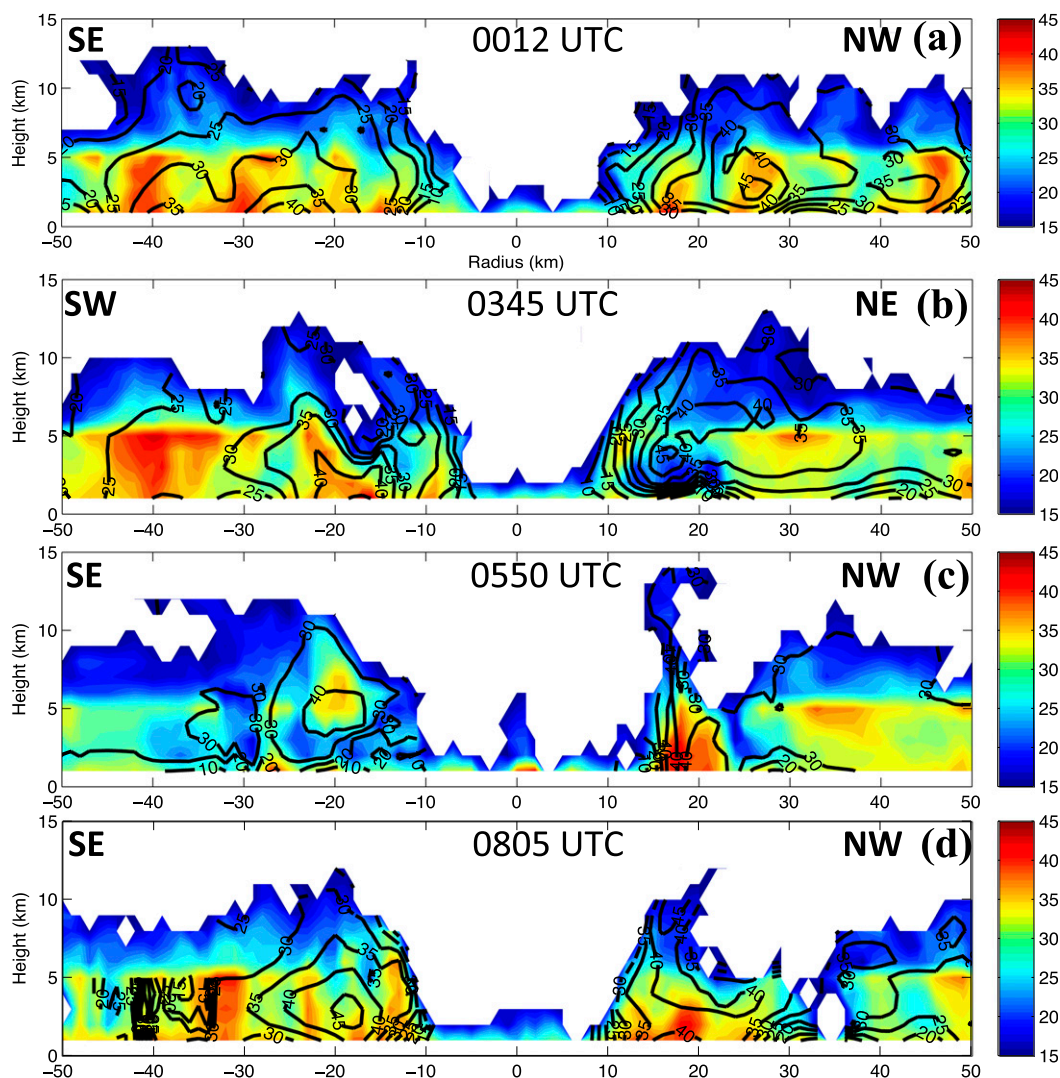


FIG. 16. HIWRAP vertical cross sections of Ku-band reflectivity (shading; dBZ) and tangential winds (contours;  $\text{m s}^{-1}$ ) at nadir for the GH overpasses centered at (a) 0012 UTC 17 Sep in southeast-to-northwest direction, (b) 0345 UTC 17 Sep in southwest-to-northeast direction, (c) 0550 UTC 17 Sep in southeast-to-northwest direction, and (d) 0805 UTC 17 Sep in southeast-to-northwest direction.

the initiation of convective towers was found to result from convergence between shear-induced asymmetries and the cyclonic flow associated with eyewall mesovortices. Reasor et al. (2009) also found observational evidence for the triggering of convective bursts through the interaction of low-level environmental flow and low-wavenumber vorticity asymmetries in the eyewall of Hurricane Guillermo (1997). The HIWRAP and WP-3D TA radar analysis described in this paper highlights a similar convergence mechanism with the addition of significant transport of anomalously warm, buoyant air from the eye into the eyewall at low levels as indicated by the HIWRAP and HAMSAR data. This additional piece of evidence linked to the formation

and maintenance of the convective bursts is supported by the trajectory analysis of a numerically simulated hurricane by Cram et al. (2007). In addition, Eastin et al. (2005) analyzed flight-level and dropsonde data in Hurricanes Guillermo (1997) and Georges (1998) and found that the low-level eye was an important source region for buoyant updrafts in the eyewall. They provided circumstantial evidence that mesovortices were the primary mechanism for the transport of the eye air into the eyewall.

The formation of a clear eye and growth of the warm core of Karl are influenced by both asymmetric and axisymmetric processes. The TA and especially HIWRAP data showed that convective-induced descent



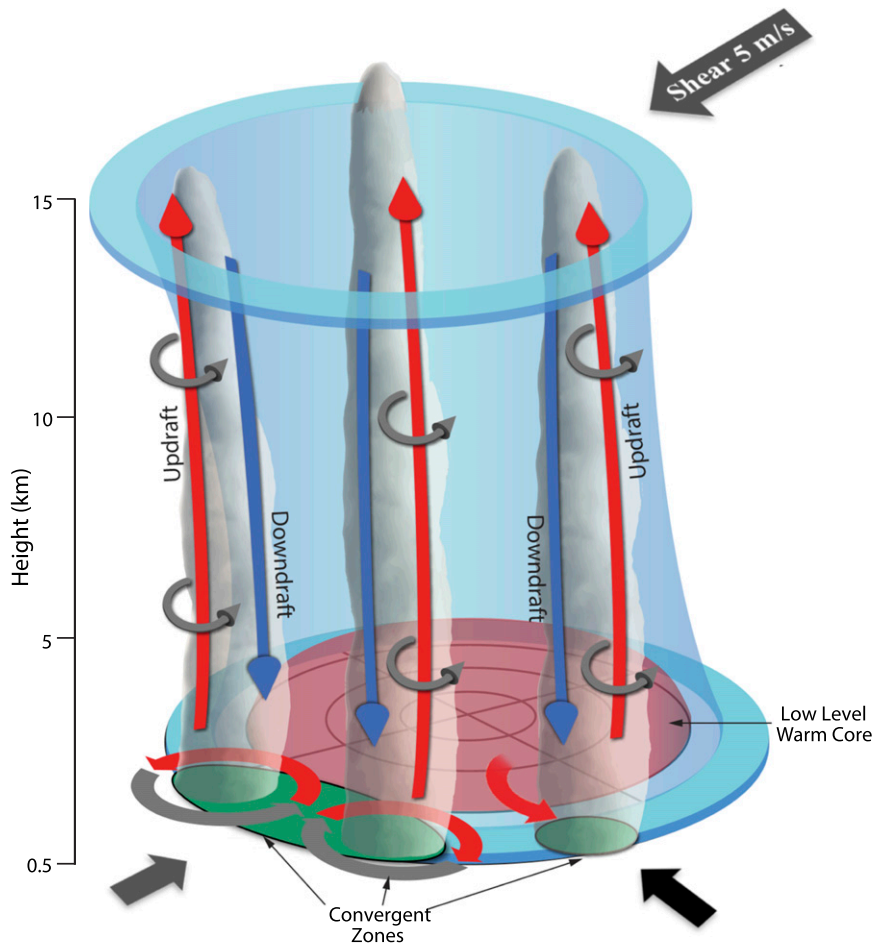


FIG. 17. Conceptual diagram highlighting the measurements and analysis from the HIWRAP, HAMSRS, and WP-3D instruments during the Hurricane Karl (2010) sampling. The arrows at lower levels represent the mesoscale flow and the arrows in the clouds represent the convective-scale flow. Red arrows indicate anomalously warm, buoyant air with blue arrows the opposite.

on the inner edge of the eyewall and in the eye itself was significant, which helps to warm and dry the eye over time. In addition, in one GH overpass the HIWRAP and HAMSRS data revealed that turbulent mixing between the eye and eyewall eroded the reflectivity on a local scale. These processes contribute largely to an asymmetric development of the eye and warm core of Karl. During the vortex response phase where the convective bursts are less pronounced and axisymmetrization of the convective anomalies is dominant, the development of the eye has a clear axisymmetric signal shown by the time series of HIWRAP data.

*Acknowledgments.* We thank Dr. Lihua Li, Matt McLinden, Martin Perrine, and Jaime Cervantes for their engineering efforts on HIWRAP during GRIP. We also thank the JPL HAMSRS team for providing

level 1B data used in this study, which was obtained from the NASA Global Hydrology Resource Center in Huntsville, Alabama. Discussions with Dr. Scott Braun were useful and helped to clarify the presentation of the data. Dr. Lin Tian helped with early HIWRAP data processing. Author Guimond and coauthors Heymsfield and Didlake were funded under Heymsfield's NASA GRIP and HS3 funding, through NASA headquarters Program Manager Dr. Ramesh Kakar. Coauthor Reasor was funded through NOAA base funds. The NASA weather program under Dr. Ramesh Kakar supported GRIP. The first author was also partially supported by the Institute of Geophysics and Planetary Physics (IGPP) at Los Alamos National Laboratory. The first author thanks Robert Kilgore for his artistic work on the conceptual diagram. Finally, we thank Rob

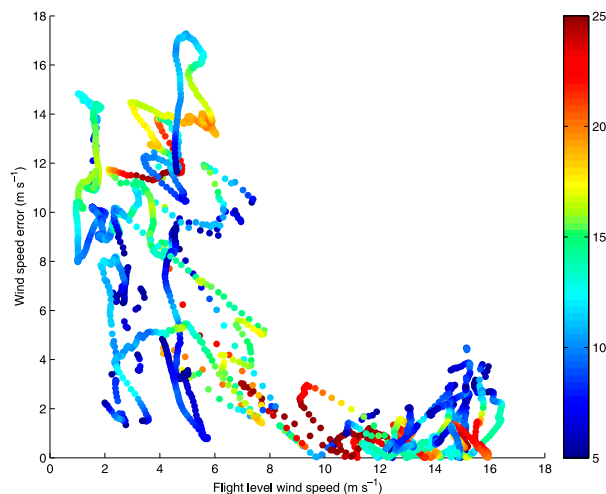


FIG. A1. Scatterplot of HIWRAP horizontal wind speed errors ( $|\text{HIWRAP} - \text{WP-3D flight level}|$ ) vs WP-3D flight-level wind speeds for the coordinated flight during HS3 on 25 Sep 2013. The points are colored by HIWRAP Ku-band reflectivity. Note the HIWRAP winds are computed using Ku-band Doppler velocities. See text for more details.

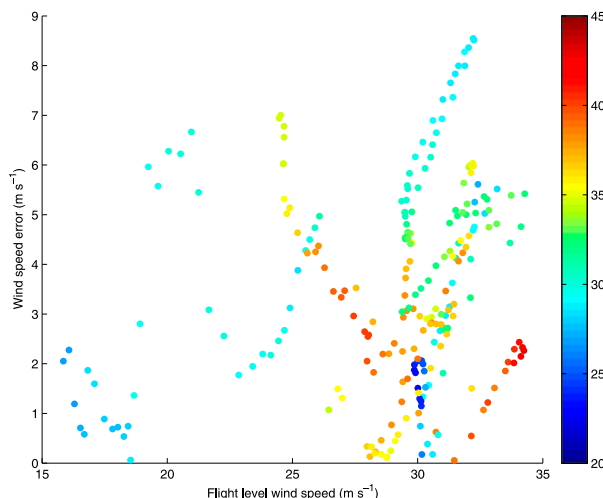


FIG. A2. As in Fig. A1, but for the coordinated flight during GRIP (sampling of Hurricane Karl at  $\sim 2040$  UTC 16 Sep 2010). The points are colored by HIWRAP Ku-band reflectivity. Note the HIWRAP winds are computed using a combination of Ku- and Ka-band Doppler velocities. See text for more details.

Rogers and two anonymous reviewers for their very helpful comments.

## APPENDIX

### Comparison of HIWRAP Wind Retrievals to Flight-Level Data

The HIWRAP radar participated in the NASA Hurricane and Severe Storm Sentinel (HS3) field campaign between the years 2012 and 2014 to study hurricane evolution. As part of this experiment, a coordinated flight between the Global Hawk and the NOAA WP-3D aircraft on 25 September 2013 allowed for the opportunity to validate the HIWRAP wind retrievals with flight-level wind data. The aircraft sampled the end of a large-scale frontal system with a mix of stratiform and weak convective precipitation.

To make the comparisons, all HIWRAP data with a time offset of  $<10$  min and space offset of  $<1$  km from the WP-3D aircraft and with reflectivity  $>5$  dBZ are retained. These data are then interpolated to the locations of the flight-level measurements (height of  $\sim 2$  km). In an attempt to match the along-track sampling of the flight-level winds (1 Hz or  $\sim 100$ – $150$  m for a typical WP-3D airspeed) with the HIWRAP wind retrieval grid (1 km) a 10-point running mean filter is applied to the flight-level winds.

Figure A1 shows a scatterplot of the horizontal wind speed error, defined as  $|\text{HIWRAP} - \text{WP-3D flight}$

level|, versus the flight-level horizontal wind speed. In this figure, HIWRAP Ku-band data are shown. There is a clear trend of lower errors for higher wind speeds. For all the points in Fig. A1 ( $N = 2727$ ) the RMSE for wind speed and direction (not shown) is  $7.8 \text{ m s}^{-1}$  and  $27^\circ$ , respectively. When considering points where the wind speed is  $>10 \text{ m s}^{-1}$  ( $N = 1077$ ) the RMSE for wind speed and direction is  $1.3 \text{ m s}^{-1}$  and  $19^\circ$ , respectively. These errors are slightly lower for Ka-band data likely because of the higher signal-to-noise ratios when compared to Ku band. For example, when the wind speed is  $>10 \text{ m s}^{-1}$  ( $N = 1321$ ) the RMSE for wind speed and direction using Ka-band data is  $1.1 \text{ m s}^{-1}$  and  $15^\circ$ , respectively. No clear reflectivity dependence is observed in Fig. A1, but the values give an indication of the intensity of precipitation sampled.

Coordination between the Global Hawk and NOAA WP-3D aircraft also occurred for one overpass of Hurricane Karl during GRIP at  $\sim 2040$  UTC 16 September 2010. The same procedures described above were applied to these data. The flight-level measurements were located between 3.5- and 3.8-km height and the time offset between the aircraft was  $\sim 2$ – $3$  min. Figure A2 shows these comparison results for the same kind of scatterplot as that in Fig. A1. A trend for lower errors with increasing wind speeds is not observed with the range of values sampled here, but a slight indication of lower errors for higher reflectivity values is somewhat apparent. For all the points in Fig. A2 ( $N = 239$ ) the RMSE for wind speed and direction (not shown) is  $4.0 \text{ m s}^{-1}$  and  $11^\circ$ , respectively.

## REFERENCES

- Braun, S., M. T. Montgomery, and Z. Pu, 2006: High-resolution simulation of Hurricane Bonnie (1998). Part I: The organization of eyewall vertical motion. *J. Atmos. Sci.*, **63**, 19–42, doi:[10.1175/JAS3598.1](https://doi.org/10.1175/JAS3598.1).
- , and Coauthors, 2013: NASA's Genesis and Rapid Intensification Processes (GRIP) field experiment. *Bull. Amer. Meteor. Soc.*, **94**, 345–363, doi:[10.1175/BAMS-D-11-00232.1](https://doi.org/10.1175/BAMS-D-11-00232.1).
- Brown, S. T., B. Lambriksen, R. F. Denning, T. Gaier, P. Kangaslahti, B. H. Lim, J. M. Tanabe, and A. B. Tanner, 2011: The High-Altitude MMIC Sounding Radiometer for the Global Hawk unmanned aerial vehicle: Instrument description and performance. *IEEE Trans. Geosci. Remote Sens.*, **49**, 3291–3301, doi:[10.1109/TGRS.2011.2125973](https://doi.org/10.1109/TGRS.2011.2125973).
- Cram, T. A., J. Persing, M. T. Montgomery, and S. A. Braun, 2007: A Lagrangian trajectory view on transport and mixing processes between the eye, eyewall, and environment using a high-resolution simulation of Hurricane Bonnie (1998). *J. Atmos. Sci.*, **64**, 1835–1856, doi:[10.1175/JAS3921.1](https://doi.org/10.1175/JAS3921.1).
- Eastin, M. D., W. M. Gray, and P. G. Black, 2005: Buoyancy of convective vertical motions in the inner core of intense hurricanes. Part II: Case studies. *Mon. Wea. Rev.*, **133**, 209–227, doi:[10.1175/MWR-2849.1](https://doi.org/10.1175/MWR-2849.1).
- Emanuel, K. A., 1986: An air–sea interaction theory for tropical cyclones. Part I: Steady-state maintenance. *J. Atmos. Sci.*, **43**, 2044–2061, doi:[10.1175/1520-0469\(1986\)043<0585:AASITF>2.0.CO;2](https://doi.org/10.1175/1520-0469(1986)043<0585:AASITF>2.0.CO;2).
- Gamache, J. F., 1997: Evaluation of a fully three-dimensional variational Doppler analysis technique. Preprints, *28th Conf. on Radar Meteorology*, Austin, TX, Amer. Meteor. Soc., 422–423.
- , 2005: Real-time dissemination of hurricane wind fields determined from airborne Doppler radar data. National Hurricane Center JHT Project Final Rep., 38 pp. [Available online at [http://www.nhc.noaa.gov/jht/2003-2005reports/DOPLRGamache\\_JHTfinalreport.pdf](http://www.nhc.noaa.gov/jht/2003-2005reports/DOPLRGamache_JHTfinalreport.pdf).]
- , F. D. Marks, and F. Roux, 1995: Comparison of three airborne Doppler sampling techniques with airborne in situ wind observations in Hurricane Gustav (1990). *J. Atmos. Oceanic Technol.*, **12**, 171–181, doi:[10.1175/1520-0426\(1995\)012<0171:COTADS>2.0.CO;2](https://doi.org/10.1175/1520-0426(1995)012<0171:COTADS>2.0.CO;2).
- Goldberg, M. D., D. S. Crosby, and L. Zhou, 2001: The limb adjustment of AMSU-A observations: Methodology and validation. *J. Appl. Meteor.*, **40**, 70–83, doi:[10.1175/1520-0450\(2001\)040<0070:TLAOAA>2.0.CO;2](https://doi.org/10.1175/1520-0450(2001)040<0070:TLAOAA>2.0.CO;2).
- Guimond, S. R., G. M. Heymsfield, and F. J. Turk, 2010: Multiscale observations of Hurricane Dennis (2005): The effects of hot towers on rapid intensification. *J. Atmos. Sci.*, **67**, 633–654, doi:[10.1175/2009JAS3119.1](https://doi.org/10.1175/2009JAS3119.1).
- , L. Tian, G. M. Heymsfield, and S. J. Frasier, 2014: Wind retrieval algorithms for the IWRAP and HIWRAP airborne Doppler radars with applications to hurricanes. *J. Atmos. Oceanic Technol.*, **31**, 1189–1215, doi:[10.1175/JTECH-D-13-00140.1](https://doi.org/10.1175/JTECH-D-13-00140.1).
- Hendricks, E. A., B. D. McNoldy, and W. H. Schubert, 2012: Observed inner-core structural variability in Hurricane Dolly (2008). *Mon. Wea. Rev.*, **140**, 4066–4077, doi:[10.1175/MWR-D-12-00018.1](https://doi.org/10.1175/MWR-D-12-00018.1).
- , W. H. Schubert, Y. Chen, H. Kuo, and M. S. Peng, 2014: Hurricane eyewall evolution in a forced shallow-water model. *J. Atmos. Sci.*, **71**, 1623–1643, doi:[10.1175/JAS-D-13-0303.1](https://doi.org/10.1175/JAS-D-13-0303.1).
- Heymsfield, G. M., J. B. Halverson, J. Simpson, L. Tian, and T. P. Bui, 2001: ER-2 Doppler radar investigations of the eyewall of Hurricane Bonnie during the Convection and Moisture Experiment-3. *J. Appl. Meteor.*, **40**, 1310–1330, doi:[10.1175/1520-0450\(2001\)040<1310:EDRIOT>2.0.CO;2](https://doi.org/10.1175/1520-0450(2001)040<1310:EDRIOT>2.0.CO;2).
- Houze, R. A., W. C. Lee, and M. M. Bell, 2009: Convective contribution to the genesis of Hurricane Ophelia (2005). *Mon. Wea. Rev.*, **137**, 2778–2800, doi:[10.1175/2009MWR2727.1](https://doi.org/10.1175/2009MWR2727.1).
- Jiang, H., 2012: The relationship between tropical cyclone intensity change and the strength of inner-core convection. *Mon. Wea. Rev.*, **140**, 1164–1176, doi:[10.1175/MWR-D-11-00134.1](https://doi.org/10.1175/MWR-D-11-00134.1).
- Kaplan, J., and M. DeMaria, 2003: Large-scale characteristics of rapidly intensifying tropical cyclones in the North Atlantic basin. *Wea. Forecasting*, **18**, 1093–1108, doi:[10.1175/1520-0434\(2003\)018<1093:LCORIT>2.0.CO;2](https://doi.org/10.1175/1520-0434(2003)018<1093:LCORIT>2.0.CO;2).
- Kelley, O. A., J. Stout, and J. B. Halverson, 2004: Tall precipitation cells in tropical cyclone eyewalls are associated with tropical cyclone intensification. *Geophys. Res. Lett.*, **31**, L24112, doi:[10.1029/2004GL021616](https://doi.org/10.1029/2004GL021616).
- Kossin, J. P., and M. D. Eastin, 2001: Two distinct regimes in the kinematic and thermodynamic structure of the hurricane eye and eyewall. *J. Atmos. Sci.*, **58**, 1079–1090, doi:[10.1175/1520-0469\(2001\)058<1079:TDRITK>2.0.CO;2](https://doi.org/10.1175/1520-0469(2001)058<1079:TDRITK>2.0.CO;2).
- , and W. H. Schubert, 2001: Mesovortices, polygonal flow patterns, and rapid pressure falls in hurricane-like vortices. *J. Atmos. Sci.*, **58**, 2196–2209, doi:[10.1175/1520-0469\(2001\)058<2196:MPPPAR>2.0.CO;2](https://doi.org/10.1175/1520-0469(2001)058<2196:MPPPAR>2.0.CO;2).
- Li, L., and Coauthors, 2016: The NASA High-Altitude Imaging Wind and Rain Airborne Profiler (HIWRAP). *IEEE Trans. Geosci. Remote Sens.*, **54**, 298–310, doi:[10.1109/TGRS.2015.2456501](https://doi.org/10.1109/TGRS.2015.2456501).
- Marks, F. D., 1985: Evolution and structure of precipitation in Hurricane Allen (1980). *Mon. Wea. Rev.*, **113**, 909–930, doi:[10.1175/1520-0493\(1985\)113<0909:EOTSOP>2.0.CO;2](https://doi.org/10.1175/1520-0493(1985)113<0909:EOTSOP>2.0.CO;2).
- Molinari, J., and D. Vollaro, 2010: Rapid intensification of a sheared tropical storm. *Mon. Wea. Rev.*, **138**, 3869–3885, doi:[10.1175/2010MWR3378.1](https://doi.org/10.1175/2010MWR3378.1).
- Montgomery, M. T., and R. J. Kallenbach, 1997: A theory for vortex Rossby waves and its application to spiral bands and intensity changes in hurricanes. *Quart. J. Roy. Meteor. Soc.*, **123**, 435–465, doi:[10.1002/qj.49712353810](https://doi.org/10.1002/qj.49712353810).
- , M. Nicholls, T. Cram, and A. Saunders, 2006: A vortical hot tower route to tropical cyclogenesis. *J. Atmos. Sci.*, **63**, 355–386, doi:[10.1175/JAS3604.1](https://doi.org/10.1175/JAS3604.1).
- Nolan, D. S., and M. T. Montgomery, 2002: Nonhydrostatic, three-dimensional perturbations to balanced, hurricane-like vortices. Part I: Linearized formulation, stability, and evolution. *J. Atmos. Sci.*, **59**, 2989–3020, doi:[10.1175/1520-0469\(2002\)059<2989:NTDPTB>2.0.CO;2](https://doi.org/10.1175/1520-0469(2002)059<2989:NTDPTB>2.0.CO;2).
- , and L. D. Grasso, 2003: Nonhydrostatic, three-dimensional perturbations to balanced, hurricane-like vortices. Part II: Symmetric response and nonlinear simulations. *J. Atmos. Sci.*, **60**, 2717–2745, doi:[10.1175/1520-0469\(2003\)060<2717:NTPTBH>2.0.CO;2](https://doi.org/10.1175/1520-0469(2003)060<2717:NTPTBH>2.0.CO;2).
- , Y. Moon, and D. P. Stern, 2007: Tropical cyclone intensification from asymmetric convection: Energetics and efficiency. *J. Atmos. Sci.*, **64**, 3377–3405, doi:[10.1175/JAS3988.1](https://doi.org/10.1175/JAS3988.1).
- Persing, J., M. T. Montgomery, J. C. McWilliams, and R. K. Smith, 2013: Asymmetric and axisymmetric dynamics of tropical cyclones. *Atmos. Chem. Phys.*, **13**, 12 299–12 341, doi:[10.5194/acp-13-12299-2013](https://doi.org/10.5194/acp-13-12299-2013).
- Reasor, P. D., M. T. Montgomery, F. D. Marks Jr., and J. F. Gamache, 2000: Low-wavenumber structure and evolution of the hurricane inner core observed by airborne

- dual-Doppler radar. *Mon. Wea. Rev.*, **128**, 1653–1680, doi:[10.1175/1520-0493\(2000\)128<1653:LWSAEO>2.0.CO;2](https://doi.org/10.1175/1520-0493(2000)128<1653:LWSAEO>2.0.CO;2).
- , —, and L. F. Bosart, 2005: Mesoscale observations of the genesis of Hurricane Dolly (1996). *J. Atmos. Sci.*, **62**, 3151–3171, doi:[10.1175/JAS3540.1](https://doi.org/10.1175/JAS3540.1).
- , M. D. Eastin, and J. F. Gamache, 2009: Rapidly intensifying Hurricane Guillermo (1997). Part I: Low-wavenumber structure and evolution. *Mon. Wea. Rev.*, **137**, 603–631, doi:[10.1175/2008MWR2487.1](https://doi.org/10.1175/2008MWR2487.1).
- , R. F. Rogers, and S. Lorsolo, 2013: Environmental flow impacts on tropical cyclone structure diagnosed from airborne Doppler radar composites. *Mon. Wea. Rev.*, **141**, 2949–2969, doi:[10.1175/MWR-D-12-00334.1](https://doi.org/10.1175/MWR-D-12-00334.1).
- Reinhart, B., and Coauthors, 2014: Understanding the relationships between lightning, cloud microphysics, and airborne radar derived storm structure during Hurricane Karl (2010). *Mon. Wea. Rev.*, **142**, 590–605, doi:[10.1175/MWR-D-13-00008.1](https://doi.org/10.1175/MWR-D-13-00008.1).
- Rogers, R. F., P. D. Reasor, and S. Lorsolo, 2013: Airborne Doppler observations of the inner-core structural differences between intensifying and steady-state tropical cyclones. *Mon. Wea. Rev.*, **141**, 2970–2991, doi:[10.1175/MWR-D-12-00357.1](https://doi.org/10.1175/MWR-D-12-00357.1).
- , —, and J. A. Zhang, 2015: Multiscale structure and evolution of Hurricane Earl (2010) during rapid intensification. *Mon. Wea. Rev.*, **143**, 536–562, doi:[10.1175/MWR-D-14-00175.1](https://doi.org/10.1175/MWR-D-14-00175.1).
- Rotunno, R., and K. A. Emanuel, 1987: An air–sea interaction theory for tropical cyclones. Part II: Evolutionary study using a nonhydrostatic axisymmetric numerical model. *J. Atmos. Sci.*, **44**, 542–561, doi:[10.1175/1520-0469\(1987\)044<0542:AAITFT>2.0.CO;2](https://doi.org/10.1175/1520-0469(1987)044<0542:AAITFT>2.0.CO;2).
- Rozoff, C. M., J. P. Kossin, W. H. Schubert, and P. J. Mulero, 2009: Internal control of hurricane intensity: The dual nature of potential vorticity mixing. *J. Atmos. Sci.*, **66**, 133–147, doi:[10.1175/2008JAS2717.1](https://doi.org/10.1175/2008JAS2717.1).
- Schubert, W. H., and J. J. Hack, 1982: Inertial stability and tropical cyclone development. *J. Atmos. Sci.*, **39**, 1687–1697, doi:[10.1175/1520-0469\(1982\)039<1687:ISATCD>2.0.CO;2](https://doi.org/10.1175/1520-0469(1982)039<1687:ISATCD>2.0.CO;2).
- , M. T. Montgomery, R. K. Taft, T. A. Guinn, S. R. Fulton, J. P. Kossin, and J. P. Edwards, 1999: Polygonal eyewalls, asymmetric eye contraction, and potential vorticity mixing in hurricanes. *J. Atmos. Sci.*, **56**, 1197–1223, doi:[10.1175/1520-0469\(1999\)056<1197:PEAECA>2.0.CO;2](https://doi.org/10.1175/1520-0469(1999)056<1197:PEAECA>2.0.CO;2).
- Shapiro, L. J., and H. E. Willoughby, 1982: The response of balanced hurricanes to local sources of heat and momentum. *J. Atmos. Sci.*, **39**, 378–394, doi:[10.1175/1520-0469\(1982\)039<0378:TROBHT>2.0.CO;2](https://doi.org/10.1175/1520-0469(1982)039<0378:TROBHT>2.0.CO;2).
- Simpson, J., J. B. Halverson, B. S. Ferrier, W. A. Petersen, R. H. Simpson, R. Blakeslee, and S. L. Durden, 1998: On the role of “hot towers” in tropical cyclone formation. *Meteor. Atmos. Phys.*, **67**, 15–35, doi:[10.1007/BF01277500](https://doi.org/10.1007/BF01277500).
- Steranka, J., E. B. Rodgers, and R. C. Gentry, 1986: The relationship between satellite-measured convective bursts and tropical cyclone intensification. *Mon. Wea. Rev.*, **114**, 1539–1546, doi:[10.1175/1520-0493\(1986\)114<1539:TRBSMC>2.0.CO;2](https://doi.org/10.1175/1520-0493(1986)114<1539:TRBSMC>2.0.CO;2).
- Stevenson, S. N., K. L. Corbosiero, and J. Molinari, 2014: The convective evolution and rapid intensification of Hurricane Earl (2010). *Mon. Wea. Rev.*, **142**, 4364–4380, doi:[10.1175/MWR-D-14-00078.1](https://doi.org/10.1175/MWR-D-14-00078.1).
- Stewart, S., 2011: Tropical cyclone report: Hurricane Karl 14–18 September 2010. National Hurricane Center Rep., 17 pp. [Available online at [http://www.nhc.noaa.gov/data/tcr/AL132010\\_Karl.pdf](http://www.nhc.noaa.gov/data/tcr/AL132010_Karl.pdf).]
- Tao, C., and H. Jiang, 2015: Distributions of shallow to very deep precipitation–convection in rapidly intensifying tropical cyclones. *J. Climate*, **28**, 8791–8824, doi:[10.1175/JCLI-D-14-00448.1](https://doi.org/10.1175/JCLI-D-14-00448.1).
- Vigh, J. L., and W. H. Schubert, 2009: Rapid development of the tropical cyclone warm core. *J. Atmos. Sci.*, **66**, 3335–3350, doi:[10.1175/2009JAS3092.1](https://doi.org/10.1175/2009JAS3092.1).
- Wang, H., and Y. Wang, 2014: A numerical study of Typhoon Megi (2010). Part I: Rapid intensification. *Mon. Wea. Rev.*, **142**, 29–48, doi:[10.1175/MWR-D-13-00070.1](https://doi.org/10.1175/MWR-D-13-00070.1).
- Willoughby, H. E., and M. B. Chelmon, 1982: Objective determination of hurricane tracks from aircraft observations. *Mon. Wea. Rev.*, **110**, 1298–1305, doi:[10.1175/1520-0493\(1982\)110<1298:ODOHTF>2.0.CO;2](https://doi.org/10.1175/1520-0493(1982)110<1298:ODOHTF>2.0.CO;2).